sck cen

Registered Office
Herrmann-Debrouxlaan 40
1160 Brussel – Belgium

Foundation of Public Utility
VAT BE 406.568.867

Research Centres
Boeretang 200
2400 Mol – Belgium

Chemin du Cyclotron 6
1348 Ottignies-Louvain-la-Neuve – Belgium

Reference N°	Creation Date	
SCK CEN/50963799	2022-10-25	
Alternative Reference N°	Revision	Version
N/A	1.0	19
ISC	Revision Status	
Public	Approved	

D.5.2 Report on ESFR, MYRRHA, and ALFRED sensitivity and impact studies.docx

Authors*
Pablo Romojaro

Review information since previous revision*		
Name	**Outcome**	**Date**
Alexey Stankovskiy	Reviewed	2022-10-24

Approval information for current revision*		
Name	**Outcome**	**Date**
Gert Van den Eynde	Approved	2022-11-14

Change log*				
Revision	**Version**	**Status**	**Date**	**Description of change**
1.0	19	Approved	2022-10-25	

**This automatically generated cover page shows references and document information as were available in the Alexandria document management system on 2022-11-14. Please refer to Alexandria for current and complete metadata, or to the document contents and/or author for additional information.*

ISC motivation
ISC was automatically assigned.

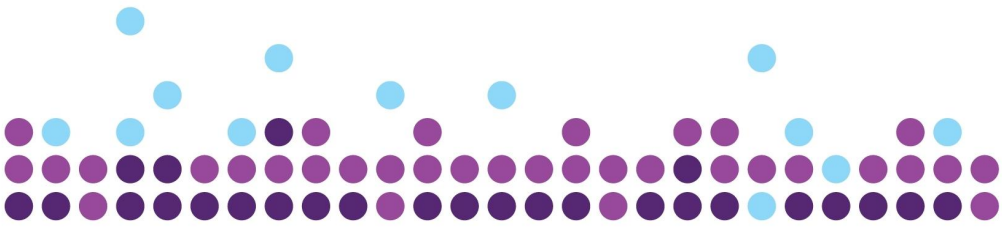

HORIZON 2020

HORIZON 2020 RESEARCH AND INNOVATION FRAMEWORK PROGRAMME OF THE EUROPEAN ATOMIC ENERGY COMMUNITY

Nuclear Fission and Radiation Protection 2018 (NFRP-2018-4)

Project acronym:	**SANDA**
Project full title:	**Solving Challenges in Nuclear Data for the Safety of European Nuclear facilities**
Grant Agreement no.:	**H2020 Grant Agreement number: 847552**

Workpackage N°:	***WP5***
Identification N°:	
Type of document:	***Deliverable***
Title:	***Report on ESFR, MYRRHA, and ALFRED sensitivity and impact studies***
Dissemination Level:	***PP***
Reference:	***SCK CEN/50963799***
Status:	***VERSION 1.0***
Comments:	

	Name	Partner	Date	Signature
Prepared by:	P. Romojaro	SCK CEN	25/10/2022	
WP leader:	R. Jacqmin	CEA		
IP Co-ordinator:	E. González	CIEMAT		

List of authors

Sonia Panizo	CIEMAT
Vicente Bécares	CIEMAT
Francisco Álvarez-Velarde	CIEMAT
Ciro Alfonso	SCK CEN / UPM
Luca Fiorito	SCK CEN
Augusto Hernández-Solís	SCK CEN
Pablo Romojaro	SCK CEN
Alexey Stankovskiy	SCK CEN
Nuria García-Herranz	UPM
Antonio Jiménez-Carrascosa	UPM
Óscar Cabellos	UPM

Table of content

Glossary of abbreviations 4

Abstract 6

Keywords 7

1. Introduction 8

2. Description of codes 9

2.1. SCALE 9

2.1.1. Methodology for S/U analysis 9

2.1.2. Processing of JEFF-libraries with AMPX 10

2.2. Serpent 2 11

2.2.1. Methodology for S/U analysis 11

2.3. SUMMON 13

3. Models 15

3.1. ESFR 15

3.2. ASTRID 15

3.3. MYRRHA 16

3.4. ALFRED 17

4. Sensitivity analysis 18

4.1. ESFR, ASTRID and ALFRED 18

4.2. MYRRHA 20

4.2.1. k_{eff} 20

4.2.2. β_{eff} 22

4.2.3. Doppler 23

4.2.4. Void 25

4.2.5. Control rod insertion 27

4.2.6. Power Peaking Factor 27

5. Uncertainty analysis 34

5.1. ESFR, ASTRID and ALFRED 34

5.2. MYRRHA 37

6. Conclusions 41

Acknowledgements 42

References 43

Annex 45

Glossary of abbreviations

ADS	Accelerator Driven System
ALFRED	Advanced Lead-cooled Fast Reactor European Demonstrator
ASTRID	Advanced Sodium Technological Reactor for Industrial Demonstration
CE	Continuous Energy
CLUTCH	Contribution-Linked eigenvalue sensitivity/Uncertainty estimation via Tracklength importance Characterization
CR	Control Rod
CSD	Control and Shutdown Devices
DSD	Diverse Shutdown Devices
EC	European Commission
ESFR	European Sodium Fast Reactor
ESFR-SMART	European Sodium Fast Reactor Safety Measures Assessment and Research Tools
ESNII	European Sustainable Nuclear Industrial Initiative
FP	Framework Programme
H2020	Horizon 2020
IFP	Iterated Fission Probability
IPS	In-Pile Section
ISC	Integrated Sensitivity Coefficients
JEFF	Joint Evaluated Fission and Fusion
LBE	Lead-Bismuth Eutectic
LFR	Lead-cooled Fast Reactor
MCNP	Monte Carlo N-Particle
MG	Multi Group
MOX	Mixed OXide
MYRRHA	Multi-purpose Hybrid Research Reactor for High-tech Applications
PPF	Power Peaking Factor
SA	SubAssembly
SAMS	Sensitivity Analysis Module for SCALE
SANDA	Supplying Accurate Nuclear Data for energy and non-energy Applications
SDF	Sensitivity Data File

SFR	Sodium-cooled Fast Reactor
SR	Safety Rod
STA	Spallation Target Assembly
S/U	Sensitivity and Uncertainty
SUMMON	Sensitivity and Uncertainty Methodology for Monte Carlo codes
TSAR	Tool for Sensitivity Analysis of Reactivity Responses
TSUNAMI	Tools for Sensitivity and Uncertainty Analysis Methodology Implementation
WP	Work Package
WPEC	Working Party on International Nuclear Data Evaluation Co-operation

Abstract

S/U analysis have been performed for the ESFR, ASTRID and ALFRED advanced reactor systems and the multi-purpose flexible irradiation facility MYRRHA, with SCALE, Serpent 2 and SUMMON codes and JEFF-3.3 nuclear data library for relevant reactor safety parameters, namely k_{eff}, β_{eff}, Doppler reactivity coefficients, void worth, reactivity worth of control rods and power peaking factor of MYRRHA.

A ranking of the most important isotopes and reactions for each parameter has been derived for all the systems. Uncertainties have been quantified and have been found to be higher than target accuracies proposed. Therefore, recommendations of nuclear data in need of improvement are given.

Keywords

Sensitivity and uncertainty; nuclear data; JEFF; advanced systems; ESFR; ASTRID; MYRRHA; ALFRED; SANDA

1. Introduction

The EC H2020 SANDA project (Supplying Accurate Nuclear Data for energy and non-energy Applications) [1] aims to enhance the quality of nuclear data by coordinating European activities in the whole nuclear data cycle, ranging from new measurements in both energy-dependent and integral experiments to evaluation, validation and dissemination activities.

In particular, the aim of WP5, Task 5.1 of the project is to evaluate the impact of nuclear data uncertainties on important design, safety and operational quantities of advanced systems. The final goal is to discuss the implications of the a priori covariance data used and to make recommendations about which nuclear data are in need of improvement and what performance gains can be expected as a consequence. These, will be communicated to the JEFF community for consideration in the next release of the JEFF nuclear data library, JEFF-4.0, planned for 2024 [2].

It is well-known that the impact of nuclear data depends on the specific design choices, even within a given "family" of systems. It is thus essential to consider different systems and to compare the results when analysing each system individually and together. Therefore, within the context of this task, Sensitivity and Uncertainty (S/U) analyses of the following advanced reactor systems, relying on already-available computational models developed under other EC-funded projects (in parentheses), have been performed:

- Conceptual sodium-cooled fast reactors (SFR): ASTRID-like (EC FP7 ESNII+ project [3]) and ESFR (EC H2020 ESFR-SMART project [4]).
- Conceptual lead-cooled fast reactors (LFR): ALFRED (EC FP7 ESNII+ project).

Moreover, S/U analyses of the multi-purpose flexible irradiation facility, MYRRHA, cooled by lead-bismuth eutectic (LBE), have been also carried out, using an updated model corresponding to the latest upgrade of the core design - version 1.8 - distributed with Ref. [5].

In this report, results from the S/U analyses carried out in Task 5.1 by CIEMAT and SCK CEN for MYRRHA, and by UPM for ASTRID, ESFR and ALFRED are summarized. Detailed description of the methodologies, models, calculations and results can be found in Refs. [6-8].

2. Description of codes

2.1. SCALE

SCALE code package [9] has been used by UPM for the S/U analyses of the ESFR, ASTRID and ALFRED advanced reactors. S/U analyses have been performed in both 33-energy group [10] and 7-energy group structures. Since impact studies aim at determining the major sources of uncertainty (isotope, reaction and energy group) in order to provide potential evaluation priorities, sensitivities in 7 energy groups (energy bands) together with a covariance matrix in 7 energy groups have been chosen to draw conclusions. The 7-energy group structure is the one proposed by M. Salvatores in NEA/WPEC-SG46 (see Ref. [11]).

The S/U methodology employed to compute the impact of nuclear data uncertainties is based on the use of TSUNAMI and TSAR modules of the SCALE code package [9]. The processing of JEFF-3.3 nuclear data library [12] for use with TSUNAMI-3D in continuous energy mode has been performed with the AMPX code, also part of the SCALE package [13].

2.1.1. *Methodology for S/U analysis*

TSUNAMI module (*Tools for Sensitivity and Uncertainty Analysis Methodology Implementation*), based on the adjoint-weighted first order perturbation theory [14], provides the sensitivity profiles (over a range of energy groups) of a model output parameter k to an input parameter α:

$$S_\alpha = \frac{\alpha}{k}\left(\frac{\partial k}{\partial \alpha}\right) \tag{1}$$

For calculating the sensitivity coefficients of the reactivity responses, the SCALE module TSAR (*Tool for Sensitivity Analysis of Reactivity Responses*) is used. From the sensitivity coefficients of the criticality constants corresponding to two configurations, $S_{\alpha,1}$ and $S_{\alpha,2}$, TSAR computes the relative sensitivity coefficient of the reactivity response as follows:

$$S_{\rho_{1\to2},\alpha} = \frac{\alpha}{|\rho_{1\to2}|}\frac{\partial \rho_{1\to2}}{\partial \alpha} = \frac{\alpha}{|\rho_{1\to2}|}\left(\frac{\partial \lambda_1}{\partial \alpha} - \frac{\partial \lambda_2}{\partial \alpha}\right) = \frac{\lambda_1 S_{\alpha,1} - \lambda_2 S_{\alpha,2}}{|\rho_{1\to2}|} \tag{2}$$

where $\rho_{1\to2}$ denotes the reactivity response and $\lambda = \frac{1}{k}$.

With the knowledge of the sensitivity profiles S_α and the relative covariance matrix V_α in a number of energy groups, SCALE performs the uncertainty analysis applying the sandwich rule within SAMS module, the *Sensitivity Analysis Module for SCALE*:

$$\sigma^2 = S_\alpha V_\alpha S_\alpha^T \tag{3}$$

TSUNAMI-3D module provides Monte Carlo-based sensitivities for 3D geometries. It can perform continuous-energy (CE) or multigroup (MG) S/U calculations making use of the 3D Monte Carlo KENO transport code in CE or MG mode respectively.

In the CE approach, sensitivities are computed during a single forward Monte Carlo neutron transport calculation. Two methods are available: the *Iterated Fission Probability* (IFP) methodology and the *Contribution-Linked eigenvalue sensitivity/Uncertainty estimation via Tracklength importance Characterization* (CLUTCH) methodology. The latter is preferred because of its greater computational efficiency and lower memory footprint compared to IFP method.

In the MG approach, sensitivities are computed from one forward and one adjoint transport calculation. The forward and adjoint flux angular moments are tallied at every energy and spatial region.

TSUNAMI-2D module provides deterministic-based sensitivities for 2D X-Y geometries, and it is based on the 2D NEWT transport code[1]. Sensitivities are calculated from one forward and one adjoint transport calculation. The forward and adjoint flux angular moments are determined from the fluxes computed in every quadrature direction, spatial region and energy group.

In this work, MG TSUNAMI-3D has been used to determine the sensitivity profiles of the full 3D heterogeneous models of innovative reactors while CE TSUNAMI-3D and TSUNAMI-2D have been employed for the bias study in Annex 1 of Ref. [8].

[1] NEWT does not solve the transport equation in 2D RZ geometries, so TSUNAMI-2D cannot provide sensitivities for RZ models.

MG TSUNAMI-3D has been chosen as a workable compromise to provide reliable results for 3D heterogeneous models due to the following reasons:

1. For the full heterogeneous 3D models, CE TSUNAMI-3D demands huge computational requirements (memory, computational time), leading to failure in some cases. This limitation was also observed for Serpent code during the ESFR-SMART project [15].
2. Although CE TSUNAMI-3D is compatible with the use of simplified RZ models, as shown in SANDA Deliverable D5.1 [16], the bias study performed in Ref. [17] shows significant discrepancies in the sensitivities of some reactivity coefficients between 3D heterogeneous and RZ models, suggesting the need of using heterogeneous models to draw reliable conclusions for reactivity parameters.

2.1.2. *Processing of JEFF-libraries with AMPX*

As aforementioned, the impact of JEFF-3.3 nuclear data uncertainties on design and safety parameters of ESFR, ASTRID and ALFRED reactors is performed with SCALE code package. The use of JEFF nuclear data libraries within SCALE system is not straight-forward and nuclear data processing must be carried out with the AMPX modular processing code, also part of the SCALE system. Some efforts have been recently made in this regard. In fact, the processing of JEFF nuclear data libraries with AMPX is being in-depth addressed in the frame of SANDA Task 4.3 and substantial progress have been already made [18]. Nonetheless, covariance data are also necessary for use with SCALE sensitivity and uncertainty analysis tools. In carrying out this Task 5.1, the JEFF-3.3 covariance matrices have been processed in both 33- and 7-group structures according to the processing route depicted in Figure 1.

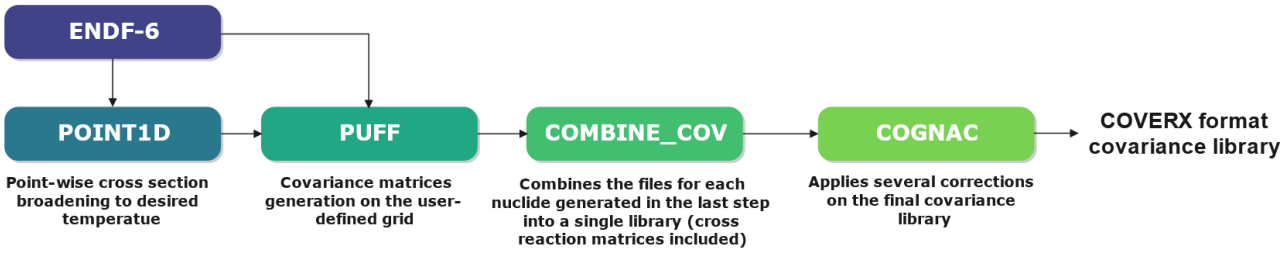

Figure 1. Covariance libraries processing route for AMPX.

The JEFF-3.3 nuclear data library contains 562 nuclides, of which 447 files including covariances. They contain information for the average number of neutrons per fission (File 31), information for the resonance parameters (File 32), information for the neutron cross sections (File 33) and information for exit energy distributions (File 35). PUFF is the main module for the generation of covariance matrices with AMPX with respect to the group-averaged cross section data. A set of files for each nuclide is generated by PUFF and then combined into a single library (including cross reaction and cross material covariance matrices, if available). Finally, several corrections are applied to the library by the COGNAC module solving potential inconsistencies such as a) redundant covariance matrices, b) relative uncertainties larger than 1, c) correlation values with absolute values larger than 1 or d) cross section data without covariance information. Then, a COVERX-formatted library is generated and readable by SCALE modules devoted to S/U analyses.

It is worth mentioning that a weighting spectrum is required for the generation of group-averaged cross section covariances. For that purpose, an optimal function for fast reactor analysis is selected. That function strongly affects to prompt fission neutron spectrum (PFNS) covariances so that the selection of an appropriate weighting spectrum is crucial.

A comprehensive comparison between AMPX and NJOY processing codes is under way in the SANDA Task 4.3 but preliminary analyses have shown a good agreement between both covariance libraries, except for threshold reactions in the 7-group structure. Uncertainty propagation exercises were carried out for the European Sodium Fast Reactor also in the frame of SANDA project [19] showing a good agreement between TSUNAMI-3D and MCNP code [20] results. In any case, presents an example concerning covariance processing with AMPX and NJOY. As it can be observed, a very good agreement is obtained in terms of relative standard deviation for both ^{238}U capture and inelastic scattering reactions.

In conclusion, a JEFF-3.3 CE neutron cross section library has been processed with AMPX along with the associated covariance library using different energy group structures. Then, in this work, uncertainty propagation for the considered advanced system is carried out based on both covariance libraries.

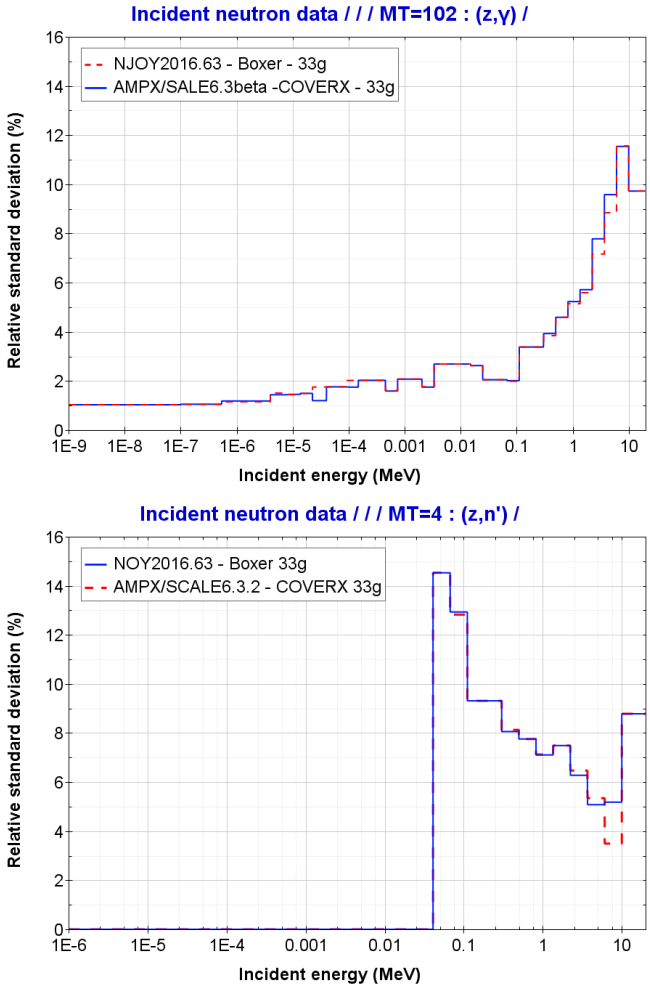

Figure 2. Group-averaged relative standard deviation for ^{238}U capture and inelastic scattering processed with NJOY2016 and AMPX.

2.2. Serpent 2

Serpent 2 [10] is a multi-purpose three-dimensional continuous-energy Monte Carlo particle code, that has been developed at VTT Technical Research Centre of Finland. It was developed to be a simplified reactor physics code, nevertheless the capabilities of the latest version, Serpent 2, extend beyond reactor modelling.

Serpent 2 has been used by SCK CEN for the S/U analyses of the multi-purpose flexible irradiation facility MYRRHA with JEFF-3.3 nuclear data library and the ECCO 33-group structure [10].

2.2.1. *Methodology for S/U analysis*

The methods implemented in Serpent 2 to calculate the sensitivity coefficients are based on linear perturbation theory using adjoint weighting, which, based on the IFP theory, interprets the adjoint flux as the neutron importance function, originally formulated by Hurwitz [21]. This method is fundamentally based on considering that the importance of an event is proportional to the neutron population present in the system during a future generation that are progeny of the original event [22]. The importance of a single particle traveling is some region of phase space is directly proportional to the population of neutrons that creates many generations after this particle ceases to be. This originating particle is known as the progenitor, and the number of progeny or descendants that it creates is known as the asymptotic population. A finite number of generations after which the progenitor's asymptotic population is approximately equal to its true asymptotic population [23, 24], are required to know a particle's importance. These are called latent generations, Figure 3 gives a simple scheme of the procedure.

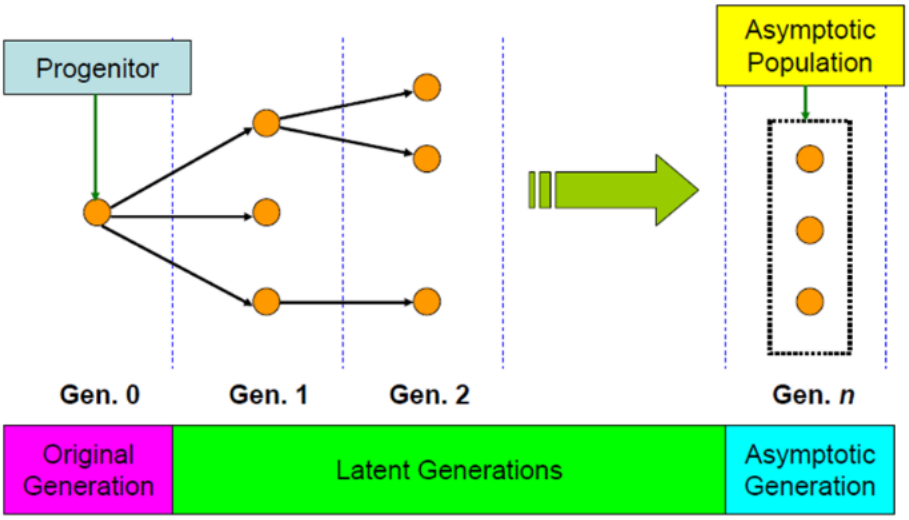

Figure 3. Iterated Fission Probability scheme [24].

The reaction rates in the first order perturbation equation are tallied by the progenitor particle ($\Sigma_x \phi$) and the asymptotic population provides an estimate for the importance of these tallies ϕ^* (see Eq. 4). Therefore, sensitivity coefficients can be calculated according to first order perturbation theory. The downside to the IFP methodology is that progenitor's reaction rate tallies for the latent generations until we reach its asymptotic generation must be storing, thus leading to a significant memory consumption.

$$RR_x = \langle \phi^*, \Sigma_x \phi \rangle \tag{4}$$

The number of latent generation necessary are usually between 5 and 10 but the MCNP code assumes 20 latent generation which is a fairly conservative number. In this work, the number of IFP latent generations has been set to 10 due to the large number of particles taken into account for the sensitivity calculations (more than 1.5×10^8). The memory footprint for the progenitor tallies can reach as much as one megabyte per progenitor particle and this memory footprint can quickly become unwieldy if many thousands of particles per generation are simulated [25].

Hereafter, such latent generations will be referred to as "IFP cycles", so as not to confuse them with "latent generations". It can be said that the IFP cycles allow the convergence of the adjoint flux for the kinetic parameters, while the so-called latent generations allow the convergence of the adjoint flux in the sensitivity calculations. Also, it is important to be clear about the difference with the inactive cycles, which represent the number of cycles that Serpent 2 uses to map the source distribution, i.e. to determine in which areas fission occurs. In this sense, they are necessary for a proper criticality or eigenvalue calculation.

This number of necessary latent generations depends on the problem. Generally 5 to 10 are required, but it is more common to take a more conservative value of 20. In this work, the number of latent generations has been set to 15 based on the analysis of previous work with the heterogeneous kernel model [19].

Moreover, it is important to note that depending on the problem, the IFP implementation can require an extensive amount of memory to store de region, nuclide, reaction and energy-dependent reaction rates for every neutron for a given number of latent generations. Therefore, it is not a viable approach for all types of problems [24].

Serpent 2 performs sensitivity calculations with a "*collision history and weight perturbation*", based upon the approach extended to Generalized Perturbation Theory, presented in detail in [26].

Figure 4 shows a simplified description of the process performed by the code. The first step consists of increasing the effective cross section by a factor f. When the reaction occurs, it is rejected with a probability of $1 - 1/f$. This virtual event is accounted for by the perturbation of the effective cross section. On the contrary, when a reaction occurs and is not rejected, it is accepted and the event is computed as real. The second step is the compression and propagation of the information to successive generations. This operation is performed by the IFP methods and it is also used for the calculation of the adjoint weighted kinetic parameters. Finally, the initial particle weight wn^0 is adjusted to compensate for the introduced bias. After each counted reaction, the weighted weight wn^* is increased if it is a real event and reduced if it is a virtual one. As noted above, during sensitivity calculations, the IFP method stores data for each progenitor neutron at each g generation. It compresses and propagates the information in M latent generations (IFP cycles) until the asymptotic population associated

with the original event is reached. Since in the framework of Monte Carlo codes a higher number of events corresponds to lower statistical errors, the IFP cycle is repeated for a certain time to reach a better estimate of the asymptotic population.

However, Serpent 2 employs a more complicated algorithm, as it takes into account an overlapping approach, where in each IFP cycle each neutron is treated as a progenitor. This allows further improvement of the statistics at a reduced extra memory cost [23].

Finally, as each response function has a different physical meaning and is governed by different phenomena, the different sensitivity coefficients have different formulations. Detailed information can be found in [7].

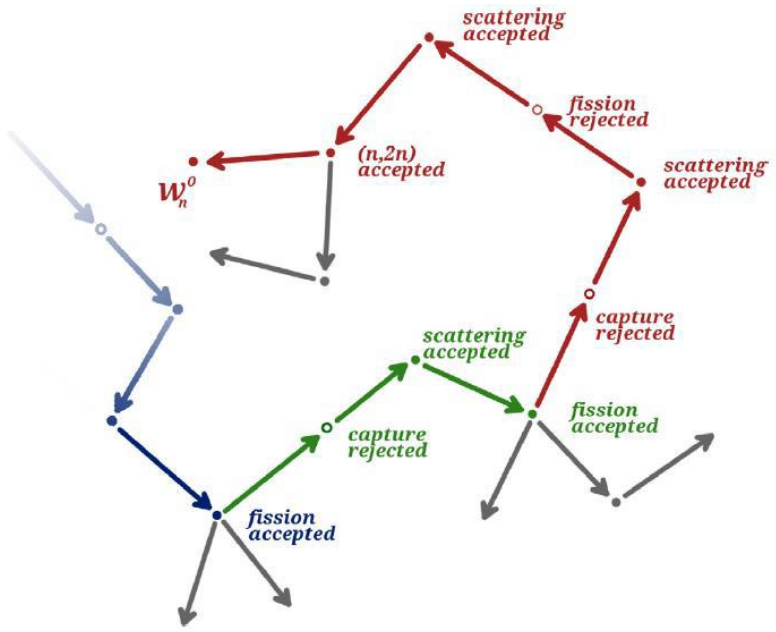

$$w_n^* \simeq w_n^0 \cdot \left(1+\frac{d\Sigma_{n,2n}}{\Sigma_{n,2n}}\right)\cdot\left(1+\frac{d\Sigma_s}{\Sigma_s}\right)\cdot\left(1-\frac{d\Sigma_f}{\Sigma_f}\right)\cdot\left(1+\frac{d\Sigma_s}{\Sigma_s}\right)\cdot\left(1-\frac{d\Sigma_c}{\Sigma_c}\right)\cdot \left(1+\frac{d\Sigma_f}{\Sigma_f}\right)\cdot\left(1+\frac{d\Sigma_s}{\Sigma_s}\right)\cdot\left(1-\frac{d\Sigma_c}{\Sigma_c}\right)\cdot\left(1+\frac{d\Sigma_f}{\Sigma_f}\right)\ldots$$

Figure 4. Collision history and weight perturbation [26].

Since Serpent 2 cannot propagate uncertainties in nuclear data, uncertainties in MYRRHA where obtained using the NDaST tool [27], which uses the same methodology as SAMS, presented in Eq. 3

2.3. SUMMON

SUMMON (*Sensitivity and Uncertainty Methodology for Monte Carlo codes*) [28] has been developed at CIEMAT. SUMMON performs sensitivity and uncertainty calculations for relevant reactor parameters using covariance matrices included in state-of-the-art nuclear data libraries and sensitivity profiles - in Sensitivity Data File (SDF) format [9] - calculated with Monte Carlo codes.

In this work, SUMMON has been used by CIEMAT to perform S/U analyses of MYRRHA. Covariance matrices from JEFF-3.3 have been used, processed in 33 energy groups [10] with NJOY21 [29], alongside sensitivity profiles calculated with the MCNP 6.2 KSEN card [20] and converted to SDF format using KSEN2sdf, a SUMMON's subroutine. This card provides sensitivity profiles only for the k_{eff}, but from them SUMMON calculates sensitivity profiles for other derived reactor parameters (β_{eff}, reactivity coefficients). However, for the case of power peaking factors, sensitivity profiles of fission rates are required, instead of sensitivity profiles of k_{eff}. While these coefficients can be in principle calculated with the PERT card of MCNP, dealing with these coefficients has yet to be implemented in SUMMON and a detailed assessment of the quality and usefulness of the results has to be performed. For this reason, S/U analyses for the power peaking factors have not been included. Specific details about the methodologies implemented in SUMMON for sensitivity calculations can be found in Refs. [28, 30, 31].

SUMMON propagates the uncertainties using the formulation presented in Eq. 3. Another point that has to be taken into account is that the variance σ_R^2 only takes into account the variance due to the uncertainty in the nuclear data, expressed in

the covariance matrix. However, when the sensitivity profiles are calculated with a Monte Carlo code, they are also affected by statistical errors. Hence, it is necessary to calculate as well the statistical error in σ_R^2. Recently, the capability for the calculation of the total statistical error has been implemented in SUMMON. It has also been compared with the result of several Monte Carlo simulations with different random number sequences. However, this last scheme is very time consuming and has only been applied to some of the parameters analyzed in this work, namely the k_{eff}, the β_{eff}, one of the void scenarios and one of the control rods insertion scenarios.

3. Models

3.1. ESFR

The ESFR core, developed in the Horizon 2020 project ESFR-SMART (2017-2022) [32], is an optimized design of the core proposed within the earlier FP7 CP-ESFR project (2009-2013) [33]. The core design modifications were aimed at improving the core map symmetry, optimizing the void effect, facilitating the corium relocation toward the corium catcher and achieving low reactivity swing in connection with a flexible breeding and minor actinide burning strategy.

Detailed specifications can be found in [34] and only main characteristics are pointed out here.

The ESFR radial layout is depicted in Figure 5 (left). The active core is composed of hexagonal subassemblies (SA) with a triangular arrangement of 271 pins. It is divided into an inner and an outer fissile fuel region with 216 and 288 SA respectively, both regions loaded with $(U,Pu)O_2$ with a Pu content of 17.99 wt% in the initial core (same initial plutonium content in the whole core). Three rings of radial reflector assemblies (264 SA) surround the active core. In addition, there are two rings for internal spent fuel storage and four rings of shielding (those assemblies were not modelled for neutronic analyses as their neutronic effect is negligible). A total of 31 corium discharge tubes, 24 Control and Shutdown Devices (CSD) and 12 Diverse Shutdown Devices (DSD) complete the core description.

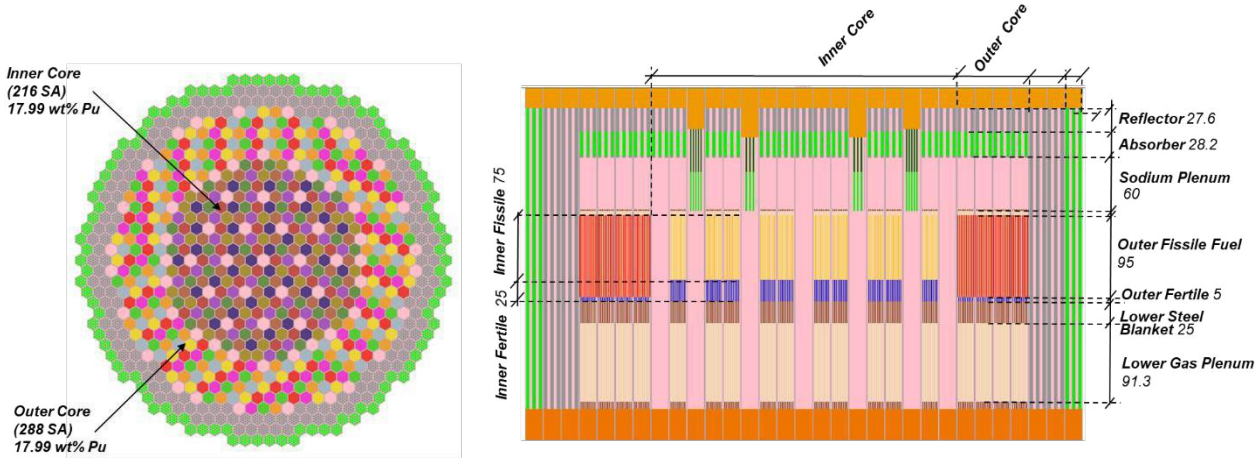

Figure 5. ESFR: developed model for KENO-VI/SCALE.

The axial layout is presented in Figure 5 (right). The height of the inner fissile region is shorter than that of the outer fissile region (75 cm versus 95 cm at cold conditions) (the radial power profile is flattened by using different fuel height in inner and outer zones). Fertile blankets are introduced below the inner and outer regions (25 and 5 cm respectively), so that the upper axial fissile boundaries are at the same height for both the inner and outer zones. Above the active core there is a large sodium plenum (60 cm) followed by a neutron absorber. The sodium plenum reflects neutrons down, when liquid, and lets neutrons fly up towards neutron absorber when voided.

3.2. ASTRID

The ASTRID-like core was investigated from a neutronic point of view within the EC FP7 ESNII+ project (2013-2017), a cross-cutting project supporting the European Sustainable Industrial Initiative [3]. It is a medium-size 1500 MW_{th} core with near zero sodium void worth at the End Of Equilibrium Cycle conditions which would prevent and mitigate severe accidents.

Detailed specifications can be found in Ref. [35] and only main characteristics are pointed out here.

The ASTRID-like radial layout is depicted in Figure 6 (left). The active core is composed of 291 hexagonal SA with a triangular arrangement of 217 pins. It is divided into an inner and an outer fuel region with 177 and 114 SA respectively, loaded with $(U,Pu)O_2$ with a Pu content of 24.3 wt% and 20.7 wt% respectively in the initial core. Three rings of radial reflector assemblies (216 SA) and four rings of radial shielding assemblies (354 SA) surround the active core. The core is controlled by 12 CSD and 6 diverse shutdown devices DSD.

The axial layout in Figure 6 (right) shows two different heights for the inner and outer fuel zones (60 cm and 90 cm respectively), with an internal axial blanket in the inner region, at the mid-plane in the core (not foreseen in the outer region). There is a thick fertile blanket below the active core. Finally, there is a large sodium plenum (30 cm) on the active core and an absorber shielding at the top, aimed at preventing neutrons from going back to the core during sodium voiding.

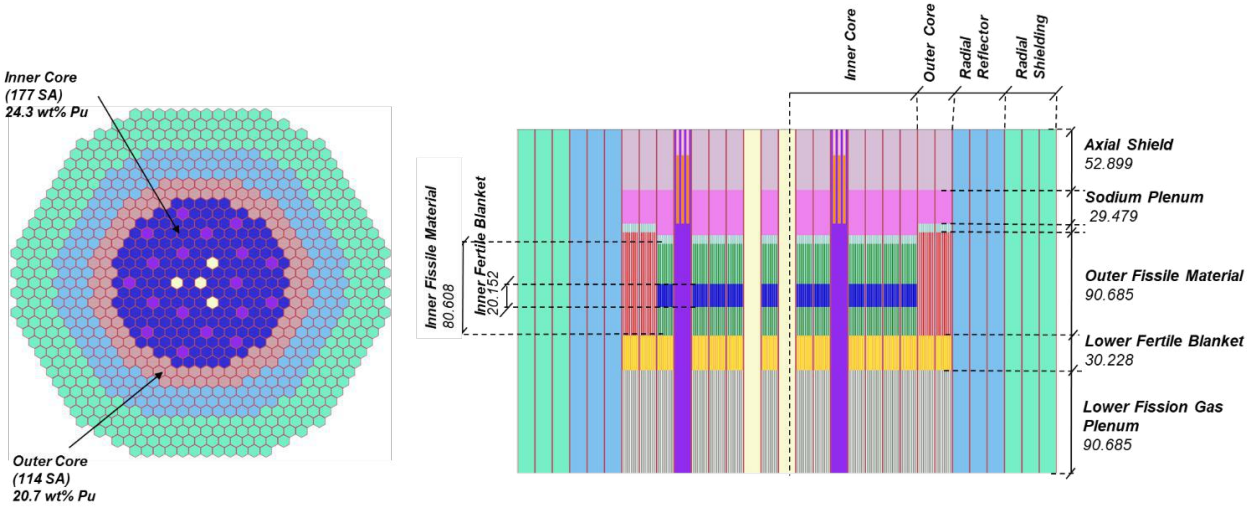

Figure 6. ASTRID-like reactor: developed model for KENO-VI/SCALE.

3.3. MYRRHA

MYRRHA (*Multi-purpose hYbrid Research Reactor for High-tech Applications*) is a multi-purpose flexible irradiation facility that has been designed to provide a research ground for Accelerator Driven System (ADS) applications. MYRRHA was conceived as a pool-type ADS reactor with a proton accelerator linked to a subcritical core fueled with MOX and cooled by LBE, with the chain reaction guaranteed by the proton beam interaction with the LBE spallation target.

Within the context of the SANDA project WP5 T5.1, SCK CEN has produced simplified versions of the MYRRHA reactor reference neutronics models [5] in MCNP for the latest neutronics design version 1.8 [36]. The core and reactor components were homogenized radially at the assembly level and vertically on a number of discrete regions. In-vessel reactor components located outside the core barrel, such as primary pumps, primary heat exchangers, fuel handling machines and fuel storages, were neglected and not modelled. Nuclide composition, densities and temperatures of the several materials were homogenized for each region using the corresponding volumes as a weighting function. The models will be used in this work to perform S/U analyses of the latest MYRRHA design, focusing on the parameters requested in Ref. [37].

The simulated MYRRHA core configurations include 163 assemblies/channels arranged in a hexagonal lattice with a central position and seven radial crowns. The assembly lattice is shrouded by a stainless steel jacket and wrapped by a cylindrical core barrel with an inner diameter of 157.0 cm and a wall thickness of 3.0 cm. The seventh crown does not contain corner assemblies to comply with the geometrical constraint imposed by the core barrel dimensions.

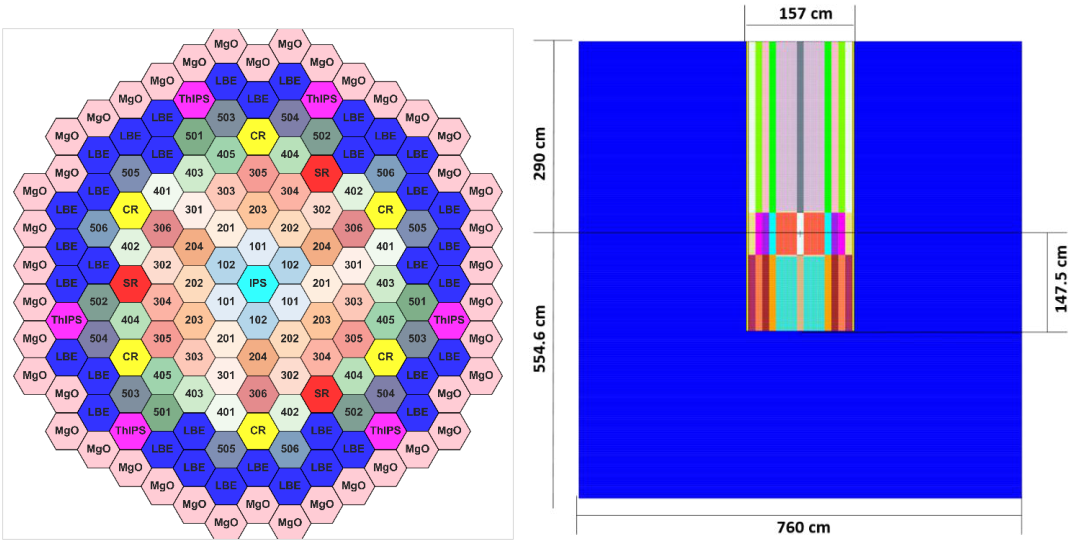

Figure 7. MYRRHA critical core: developed model for MCNP.

Both the critical (Figure 7) and subcritical layout (Ref. [5]) include:

- hexagonal fuel assemblies consisting of 127 fuel elements with highly enriched MOX fuel. Each fuel element contains a fuel vertical column 65.0 cm long that defines the axial center of the model;

- boron carbide B_4C control rod (CR) bundles;
- in-pile sections (IPSs) for material testing and experiments with fast neutron fluxes;
- in-pile sections for radioisotope production, also called thermal islands;
- dummy assemblies filled with LBE;
- reflector assemblies with bundles of magnesium oxide rods.

A spallation target assembly (STA) is located in the central channel of the subcritical core layouts and hosts the accelerator proton beam tube and window. Safety rods (SRs) are included in the critical layout as a redundant and diversified emergency shutdown system that is complementary to the CRs.

In this work, S/U analyses have been performed for the critical core configuration only. MCNP model has been also translated to Serpent 2 (details can be found in Ref. [7]).

3.4. ALFRED

The Advanced Lead-cooled Fast Reactor European Demonstrator (ALFRED) core design considered in this work was the one investigated within the EC FP7 ESNII+ project (2013-2017). ALFRED is a 300 MW_{th} small-size pool type reactor cooled by pure lead.

The ALFRED radial layout is depicted in Figure 8 (left). The active core is composed of 171 hexagonal subassemblies with a triangular arrangement of 127 pins. It is divided into an inner and an outer fissile fuel region with 57 and 114 SA respectively loaded with $(U,Pu)O_2$ with a higher enrichment in the outer region to flatten the power distribution. Two rings of reflector assemblies surround the active core. The core is controlled by 12 control rods for power regulation and reactivity swing compensation and 4 safety rods for shutdown purposes. The axial layout is depicted in Figure 8 (right).

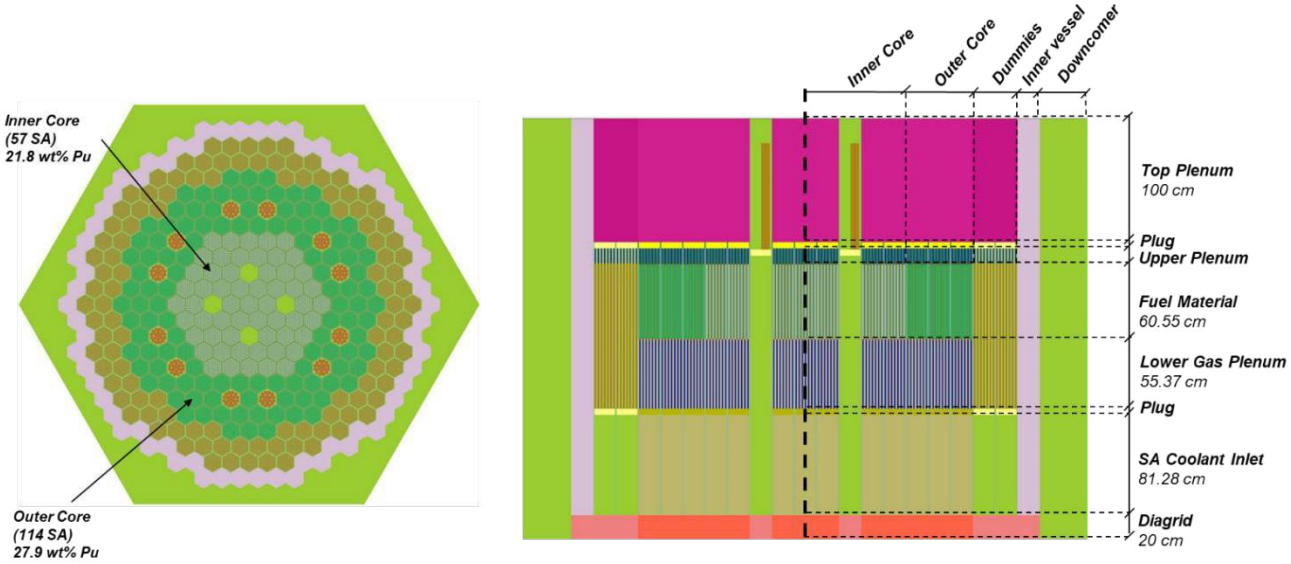

Figure 8. ALFRED: developed model for KENO-VI/SCALE.

Detailed specifications can be found in [38]. It is worth it to mention that these core specifications differ from the ones recently presented by ENEA in [39, 40]; among others, a slightly smaller core is defined (56 and 78 SA loaded in the inner and outer regions respectively).

4. Sensitivity analysis

4.1. ESFR, ASTRID and ALFRED

S/U results for the multiplication factor k_{eff} and reactivity responses of the three advanced systems are jointly presented in order to explore common and different behaviour. Reactivity responses correspond to:

- Fuel Doppler effect: a change of ±300 K from reference fuel temperature (in both inner and outer regions) has been simulated for ESFR (+300 K only) and ALFRED. Both scenarios are presented to highlight the different related uncertainties; they are relevant for example for Unprotected Transients of Over-Power or Unprotected Loss Of Off-site Power [41] respectively.
- Coolant density effect: scenarios in which coolant density decreases with respect to the nominal values by 100% - sodium voiding - in ESFR and ASTRID-like (in both fuel active regions and sodium plenum) and 20% in ALFRED (in inner active region) have been simulated. Moreover, results corresponding to different scenarios of partial voiding are also presented for ASTRID-like in Annex 3 of Ref. [8].
- Control rods reactivity worth: a perturbed scenario where control rods move from a completely extracted to a completely inserted position is simulated.

The nominal results obtained for the analysed reactor integral responses are presented in Table 1.

Table 1. Nominal values of integral responses for ESFR, ASTRID and ALFRED.

Reactor	Response	Value ± Std. Dev.
ESFR	k_{eff}	1.004992 ± 9 pcm
	Coolant density (full void)	989 ± 12 pcm
	Doppler+300K	-148 ± 13 pcm
	Control	-5420 ± 13 pcm
ASTRID	k_{eff}	1.00779 ± 8 pcm
	Coolant density (full void)	-536 ± 12 pcm
ALFRED	k_{eff}	0.99904 ± 10 pcm
	Coolant density (-20% inner region)	193 ± 13 pcm
	Doppler+300K	-112 ± 14 pcm
	Doppler-300K	188 ± 13 pcm

The highest Integrated Sensitivity Coefficients (ISC) for the most important nuclides and reactions (quantities) for the integral responses are given in Table 2 - Table 5:

- Sensitivities in k_{eff} are similar for the three reactors. The highest values correspond to Pu isotopes and ^{238}U, being the top sensitivities ^{239}Pu nubar and fission and ^{238}U(n,γ); then, nubar and fission for ^{238}U, ^{241}Pu and ^{240}Pu. Coolant and structural materials play a less important role, being scattering reactions of ^{56}Fe, ^{16}O, ^{23}Na and Pb isotopes the most significant ones, together with capture reaction of ^{56}Fe.
- Although Doppler sensitivities differ for SFR and LFR reactors, ^{239}Pu and ^{238}U cross sections are very relevant for all scenarios. Doppler effect is more sensitive to ^{238}U (n,n') and ^{238}U (n,γ) following a temperature increase than following a temperature decrease, in which case ^{238}U elastic scattering (el.) and ^{238}U nubar turn out to be the most relevant ^{238}U reactions. With respect to non-actinide isotopes, elastic scattering cross sections of ^{16}O and ^{56}Fe are significant, although the computed TSUNAMI-3D-based sensitivities exhibit large statistical deviations, being therefore not very reliable.
- Coolant density effect is again very sensitive to ^{239}Pu and ^{238}U cross sections for the three reactors, as well as to elastic scattering of ^{56}Fe. Moreover scattering cross sections of ^{23}Na are relevant for SFR and ^{206}Pb (n,n') for LFR (inelastic scattering of ^{207}Pb and ^{208}Pb are ranked as low as 12th and 16th).
- Control rod worth is very sensitive to the ^{10}B (n,α) cross-section (boron is the absorbing material in the control rods).

Sensitivity profiles of critical quantities are provided in Annex.

Table 2. Reactions with the largest values of the ISC for k_{eff} (top 10 sensitivities together with the largest values corresponding to coolant and structural materials) for ESFR, ASTRID and ALFRED.

ESFR			ASTRID			ALFRED		
Quantity	**ISC (%/%)**	**Std. Dev.**	**Quantity**	**ISC (%/%)**	**Std. Dev.**	**Quantity**	**ISC (%/%)**	**Std. Dev.**
^{239}Pu ν	6.39E-01 ±	8.9E-06	^{239}Pu ν	6.71E-01 ±	6.9E-06	^{239}Pu ν	6.91E-01 ±	1.1E-05
^{239}Pu (n,f)	4.76E-01 ±	3.0E-05	^{239}Pu (n,f)	4.90E-01 ±	2.9E-05	^{239}Pu (n,f)	4.97E-01 ±	3.8E-05
^{238}U (n,γ)	-2.02E-01 ±	3.7E-05	^{238}U (n,γ)	-2.01E-01 ±	3.1E-05	^{238}U (n,γ)	-1.52E-01 ±	3.0E-05
^{238}U ν	1.28E-01 ±	4.0E-06	^{238}U ν	1.19E-01 ±	2.6E-06	^{241}Pu ν	9.35E-02 ±	1.5E-06
^{241}Pu ν	1.01E-01 ±	1.5E-06	^{241}Pu ν	9.29E-02 ±	1.1E-06	^{238}U ν	8.51E-02 ±	3.1E-06
^{240}Pu ν	7.96E-02 ±	1.4E-06	^{240}Pu ν	7.30E-02 ±	1.0E-06	^{240}Pu ν	8.03E-02 ±	1.5E-06
^{238}U (n,f)	7.67E-02 ±	1.6E-05	^{238}U (n,f)	7.22E-02 ±	1.3E-05	^{241}Pu (n,f)	6.80E-02 ±	5.3E-06
^{241}Pu (n,f)	7.60E-02 ±	4.9E-06	^{241}Pu (n,f)	6.83E-02 ±	4.2E-06	^{240}Pu (n,f)	5.53E-02 ±	5.2E-06
^{238}U (n,n')	-7.09E-02 ±	1.5E-04	^{238}U (n,n')	-5.88E-02 ±	1.1E-04	^{238}U (n,f)	5.22E-02 ±	1.2E-05
^{16}O el.	-5.66E-02 ±	8.4E-04	^{240}Pu (n,f)	5.03E-02 ±	4.3E-06	^{239}Pu (n,γ)	-4.87E-02 ±	9.7E-06
^{56}Fe (n,n')	-2.09E-02 ±	5.6E-05	^{16}O el.	-4.36E-02 ±	7.1E-04	^{208}Pb el.	3.39E-02 ±	1.4E-04
^{56}Fe (n,γ)	-1.02E-02 ±	2.4E-06	^{56}Fe (n,n')	-1.92E-02 ±	5.8E-05	^{207}Pb el.	1.45E-02 ±	6.0E-05
^{23}Na (n,n')	-8.43E-03 ±	2.7E-05	^{56}Fe (n,γ)	-1.26E-02 ±	2.7E-06	^{206}Pb el.	1.39E-02 ±	6.0E-05
^{56}Fe el.	6.90E-03 ±	3.7E-04	^{56}Fe el.	1.00E-02 ±	2.8E-04	^{56}Fe (n,γ)	-1.35E-02 ±	2.5E-06
^{52}Cr (n,n')	-4.22E-03 ±	8.6E-06	^{23}Na el.	1.02E-02 ±	2.9E-04	^{56}Fe (n,n')	-1.29E-02 ±	5.3E-05
^{23}Na el.	3.85E-03 ±	3.3E-04	^{23}Na (n,n')	-7.18E-03 ±	2.4E-05	^{56}Fe el.	8.60E-03 ±	2.6E-04

Table 3. Reactions with the largest values of the ISC for Doppler effect (top 10 sensitivities) for ESFR, ASTRID and ALFRED.

	ESFR			ALFRED		
	Quantity	**ISC (%/%)**	**Std. Dev.**	**Quantity**	**ISC (%/%)**	**Std. Dev.**
Doppler +300K	^{239}Pu (n,f)	6.91E-01 ±	7.9E-02 (11%)	^{239}Pu (n,f)	1.15E+00 ±	4.9E-02 (4%)
	^{239}Pu ν	4.14E-01 ±	7.6E-02 (18%)	^{239}Pu ν	6.48E-01 ±	1.4E-02 (2%)
	^{56}Fe el.	3.68E-01 ±	9.7E-01 (264%)	^{238}U (n,n')	-5.83E-01 ±	1.8E-01 (30%)
	^{238}U ν	3.11E-01 ±	5.3E-02 (17%)	^{16}O el.	-5.49E-01 ±	1.0E+0 (191%)
	^{238}U (n,f)	2.77E-01 ±	5.4E-02 (20%)	^{238}U (n,γ)	-4.24E-01 ±	3.8E-02 (9%)
	^{239}Pu (n, γ)	2.10E-01 ±	1.1E-02 (5%)	^{56}Fe el.	-3.43E-01 ±	3.3E-01 (97%)
	^{240}Pu ν	1.94E-01 ±	4.2E-02 (21%)	^{238}U el.	-3.31E-01 ±	1.0E-01 (31%)
	^{240}Pu (n,f)	1.86E-01 ±	4.2E-02 (22%)	^{239}Pu (n, γ)	2.78E-01 ±	1.2E-02 (4%)
	^{238}U el.	1.80E-01 ±	8.8E-01 (490%)	^{56}Fe (n,n')	-1.93E-01 ±	6.7E-02 (34%)
	^{241}Pu (n,f)	1.41E-01 ±	4.7E-02 (33%)	^{240}Pu ν	1.65E-01 ±	2.0E-03 (1%)
Doppler -300K				^{239}Pu (n,f)	-1.11E+00 ±	2.9E-02 (3%)
				^{16}O el.	7.83E-01 ±	6.4E-01 (80%)
				^{239}Pu ν	-6.15E-01 ±	7.7E-03 (1%)
				^{239}Pu (n, γ)	-3.42E-01 ±	7.3E-03 (2%)
				^{238}U el.	2.83E-01 ±	6.1E-02 (22%)
				^{238}U ν	-1.92E-01 ±	2.2E-03 (1%)
				^{238}U (n,n')	1.71E-01 ±	1.0E-01 (61%)
				^{240}Pu ν	-1.60E-01 ±	1.0E-03 (1%)
				^{238}U (n,f)	-1.52E-01 ±	8.6E-03 (6%)
				^{240}Pu (n,f)	-1.43E-01 ±	3.9E-03 (3%)

Table 4. Reactions with the largest values of the ISC for coolant density (top 10 sensitivities) for ESFR, ASTRID and ALFRED.

ESFR				ASTRID				ALFRED			
Quantity	**ISC (%/%)**		**Std. Dev.**	**Quantity**	**ISC (%/%)**		**Std. Dev.**	**Quantity**	**ISC (%/%)**		**Std. Dev.**
^{239}Pu ν	-1.26E+00	±	1.1E-02	^{238}U ν	1.51E+00	±	7.4E-04	^{239}Pu ν	-1.56E+00	±	7.7E-03
^{238}U (n,γ)	9.94E-01	±	5.2E-03	^{238}U (n,γ)	1.10E+00	±	7.9E-03	^{239}Pu (n,f)	-1.15E+00	±	2.8E-02
^{239}Pu (n,f)	-9.73E-01	±	1.1E-02	^{239}Pu (n,γ)	1.10E+00	±	2.1E-03	^{238}U (n,γ)	8.51E-01	±	2.2E-02
^{23}Na el.	7.64E-01	±	8.1E-02	^{56}Fe el.	1.07E+00	±	7.3E-02	^{238}U ν	7.16E-01	±	2.3E-03
^{23}Na (n,n')	6.04E-01	±	4.7E-03	^{238}U (n,f)	9.49E-01	±	3.6E-03	^{238}U (n,n')	-4.74E-01	±	1.0E-01
^{239}Pu (n,γ)	5.16E-01	±	1.6E-03	^{238}U (n,n')	-9.31E-01	±	3.6E-02	^{238}U (n,f)	3.97E-01	±	8.4E-03
^{241}Pu ν	-4.84E-01	±	7.1E-03	^{23}Na (n,n')	8.95E-01	±	5.4E-03	^{206}Pb (n,n')	3.33E-01	±	1.9E-02
^{56}Fe el.	4.64E-01	±	1.4E-01	^{23}Na el.	-8.68E-01	±	6.5E-02	^{241}Pu ν	-3.03E-01	±	1.1E-03
^{238}U ν	3.84E-01	±	7.9E-03	^{239}Pu ν	-6.78E-01	±	1.9E-03	^{239}Pu (n,γ)	2.44E-01	±	7.0E-03
^{238}U (n,n')	-3.82E-01	±	2.1E-02	^{241}Pu ν	-6.02E-01	±	2.9E-04	^{16}O el.	-2.36E-01	±	6.0E-01

Table 5. Reactions with the largest values of the ISC for control rod worth (top 10 sensitivities) for ESFR, ASTRID and ALFRED.

ESFR			
Quantity	**ISC (%/%)**		**Std. Dev.**
^{239}Pu (n,f)	4.38E-01	±	2.2E-03
^{239}Pu ν	4.11E-01	±	2.2E-03
^{16}O el.	2.56E-01	±	2.3E-02
^{238}U ν	2.48E-01	±	1.5E-03
^{10}B (n,α)	-2.36E-01	±	2.5E-04
^{238}U (n,f)	2.02E-01	±	1.6E-03
^{238}U (n,γ)	1.68E-01	±	1.0E-03
^{56}Fe el.	1.60E-01	±	2.9E-02
^{240}Pu ν	1.50E-01	±	1.2E-03
^{240}Pu (n,f)	1.32E-01	±	1.2E-03

4.2. MYRRHA

The following neutronics parameters were selected by SCK CEN for the analysis in Ref. [37]:

- k_{eff},
- β_{eff},
- Doppler coefficient at 600 K, 900 K, 1200 K, 1500 K, 1800 K, 2100 K, 2400 K and 3000 K;
- Void coefficient: see Ref. [37];
- Control rod insertion: total worth;
- Power Peaking Factor (PPF), F_q:

$$F_q = \frac{q_{MAX}}{\bar{q}} = \frac{q_{MAX}}{\frac{1}{N}\sum_i q_i} \quad (5)$$

where $q_{MAX}$is the assembly with the maximum power density and $\bar{q}$ is the average power density of the core.

4.2.1. k_{eff}

The value of the effective neutron multiplication factor obtained for the MYRRHA homogenized model with MCNP code is:

$$k_{eff} = 1.01542 \pm 0.00003$$

Serpent 2 results agree within the statistical uncertainty with the calculated k_{eff} with MCNP.

Figure 9 shows a comparison between the sensitivities in k_{eff} obtained with Serpent 2 (HOMOG) and results from Ref. [30] (CHANDA) with the previous version of the model (v1.6). Figure 10 shows the sensitivity profile of the first 5 contributors as sensitivity per unit of lethargy as a function of energy. In Table 6, ISC obtained with MCNP code are presented.

Good agreement is found in k_{eff} sensitivities for MYRRHA v1.6 and v1.8. Existing differences are mainly due to changes in the geometry of the core (new version is smaller) and differences in the composition of certain materials such as the reflector. Statistical errors associated with each sensitivity coefficient have not been included because they are comparatively small with respect to the mean value. Good agreement is also found with sensitivity coefficients calculated with MCNP for MYRRHA and the values presented for ALFRED in Table 2. Overall, the highest sensitivities correspond to nubar, fission and capture in Pu isotopes and ^{238}U. Similar to ALFRED, coolant isotopes also play and important role. In MYRRHA, sensitivity in k_{eff} for elastic scattering in ^{209}Bi is larger than the sensitivity for elastic scattering in ^{208}Pb in ALFRED, since ^{209}Bi constitutes 55.5% of the LBE and has larger resonances which start at lower energies than ^{208}Pb.

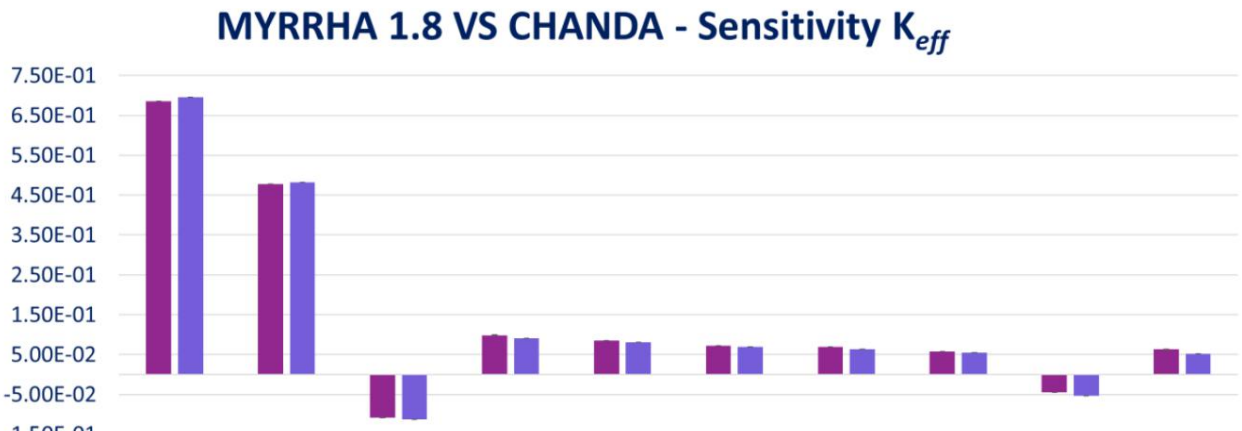

	nubar Pu_239	fiss Pu_239	capt U_238	nubar Pu_241	nubar Pu_240	nubar U_238	fiss Pu_241	fiss Pu_240	capt Pu_239	ela scat Bi_209
HOMOG	6.85E-01	4.77E-01	-1.08E-01	9.89E-02	8.49E-02	7.22E-02	7.00E-02	5.76E-02	-4.41E-02	6.29E-02
CHANDA	6.96E-01	4.82E-01	-1.12E-01	9.10E-02	8.10E-02	7.00E-02	6.40E-02	5.50E-02	-5.30E-02	5.20E-02

Figure 9. Comparison of k_{eff} ISC MYRRHA v1.8 vs v1.6 with the top 10 relevant neutron-induced nuclear data using the JEFF-3.3 library with Serpent 2.

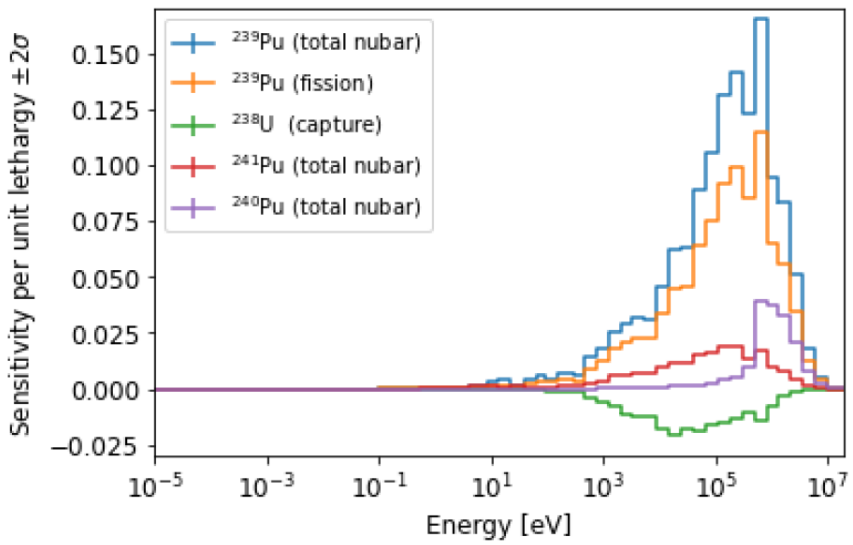

Figure 10. Top 5 energy dependent sensitivity profiles for k_{eff} in MYRRHA with Serpent 2.

Table 6. ISC for the major contributions to the k_{eff} uncertainty due to nuclear data in MYRRHA. ISC obtained with MCNP and JEFF-3.3 library.

MCNP - k_{eff}			
Quantity	**ISC (%/%)**		**Std. Dev.**
^{239}Pu $\bar{\upsilon}_p$	6.835E-01	±	4.350E-04
^{239}Pu (n,f)	4.771E-01	±	4.434E-04
^{238}U (n,γ)	-1.085E-01	±	6.078E-05
^{241}Pu $\bar{\upsilon}_p$	9.844E-02	±	7.157E-05
^{240}Pu $\bar{\upsilon}_p$	8.467E-02	±	7.394E-05
^{238}U $\bar{\upsilon}_p$	7.107E-02	±	9.526E-05
^{241}Pu (n,f)	6.993E-02	±	7.337E-05

4.2.2. β_{eff}

The value of the effective delayed neutron fraction obtained for the MYRRHA homogenized model with Serpent 2 code is:

$$\beta_{eff} = 337 \pm 1 \text{ pcm}$$

Results with Serpent 2 are in perfect agreement with the bias obtained between different calculation methods in SUMMON reported in Ref. [6].

Once again, Figure 11 shows a comparison between the sensitivities in k_{eff} obtained with Serpent 2 (HOMOG) and results from Ref. [30] (CHANDA) with the previous version of the model (v1.6). Figure 12 shows the sensitivity profile of the first 5 contributors as sensitivity per unit of lethargy as a function of energy. In Table 7, ISC obtained with SUMMON using Chiba's method [42] are presented.

Sensitivity analysis of β_{eff} provides complementary information to the k_{eff} for other quantities. As such, it can be seen in Figure 11, Figure 12 and Table 7 that the highest sensitivity of β_{eff} is to the average number of delayed and prompt neutrons. Values calculated for both MYRRHA versions and with Serpent 2 and SUMMON are in good agreement.

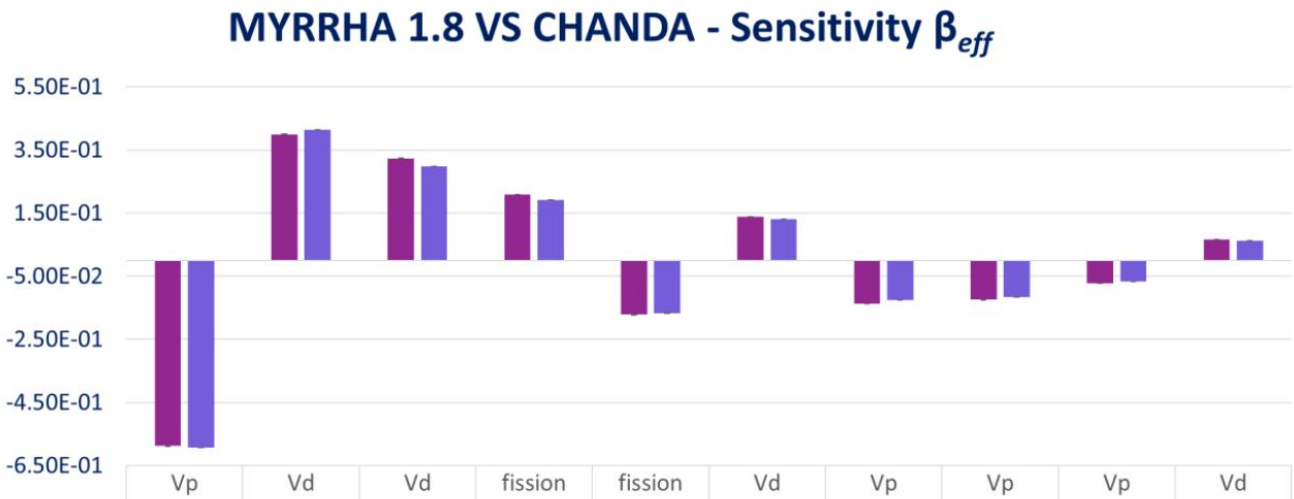

	Vp Pu_239	Vd Pu_239	Vd U_238	fission U_238	fission Pu_239	Vd Pu_241	Vp U_238	Vp Pu_240	Vp Pu_241	Vd Pu_240
HOMOG	-5.88E-01	3.99E-01	3.23E-01	2.08E-01	-1.73E-01	1.39E-01	-1.37E-01	-1.25E-01	-7.26E-02	6.64E-02
CHANDA	-5.94E-01	4.13E-01	2.97E-01	1.92E-01	-1.67E-01	1.31E-01	-1.26E-01	-1.16E-01	-6.80E-02	6.30E-02

Figure 11. Comparison of β_{eff} ISC MYRRHA 1.8 vs 1.6 with the top 10 relevant neutron-induced nuclear using the JEFF-3.3 library with Serpent 2.

A strong positive sensitivity is observed to the average number of delayed neutrons $\bar{\upsilon}_d$, since β_{eff} is the effective delayed neutron fraction, i.e. the fraction of delayed neutrons in the core that can initiate fission events, and if the number of delayed neutrons increases, so does the fraction of them that can produce fission reactions. On the other hand, there is a strong negative sensitivity of β_{eff} to the average number of prompt neutrons, $\bar{\upsilon}_p$. According to Bretscher's method [43]:

$$\beta_{eff} \cong 1 - \frac{k_p}{k} \quad (6)$$

which, developed further, gives

$$1-\frac{k_p}{k}=\frac{k-k_p}{k}=\frac{k_d}{k_p+k_d}\approx\frac{\bar{\upsilon}_d}{\bar{\upsilon}_p+\bar{\upsilon}_d}\Rightarrow S_{\bar{\upsilon}_p}^{\beta_{eff}}=\frac{\partial\beta_{eff}}{\partial\bar{\upsilon}_p}=-\frac{\bar{\upsilon}_d}{{\bar{\upsilon}_p}^2} \tag{7}$$

Since υ_p and υ_d are positive, sensitivity to υ_p is inheritably negative. Moreover, from the physical point of view, υ_p and υ_d are competitive reactions. If υ_p increases, the system will become more supercritical removing the dependence on delayed neutrons to maintain criticality (by means of fissions), making the sensitivity of β_{eff} to υ_p negative.

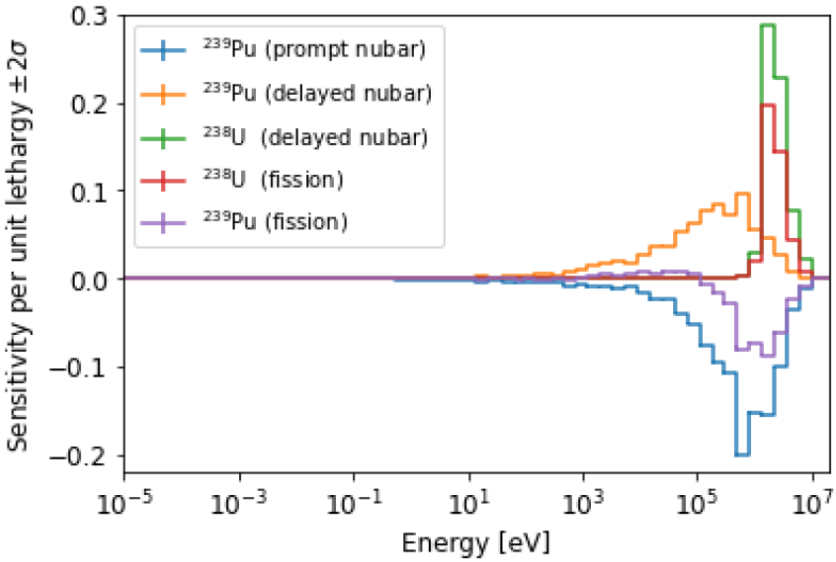

Figure 12. Top 5 energy dependent sensitivity profiles for β_{eff} in MYRRHA with Serpent 2.

Table 7. ISC for the major contributions to the β_{eff} uncertainty due to nuclear data in MYRRHA. ISC obtained with SUMMON using Chiba's method and JEFF-3.3 library.

SUMMON - β_{eff}			
Quantity	**ISC (%/%)**		**Std. Dev.**
^{239}Pu $\bar{\upsilon}_p$	-5.859E-01	±	0.000E+00
^{239}Pu $\bar{\upsilon}_d$	4.001E-01	±	2.350E-03
^{238}U $\bar{\upsilon}_d$	3.052E-01	±	1.345E-03
^{238}U (n,f)	1.976E-01	±	5.098E-03
^{239}Pu (n,f)	-1.679E-01	±	2.054E-02
^{241}Pu $\bar{\upsilon}_d$	1.404E-01	±	1.034E-03
^{238}U $\bar{\upsilon}_p$	-1.289E-01	±	4.347E-06
^{240}Pu $\bar{\upsilon}_p$	-1.199E-01	±	2.386E-05

4.2.3. Doppler

A more detailed analysis compared to Serpent 2 (Ref. [7]) has been performed with SUMMON for the Doppler coefficient in MYRRHA, therefore in this Section, only results obtained with SUMMON are presented.

In this work, the Doppler effect was studied for the 8 different temperatures listed in Table 8. These temperature changes only affect the fuel materials. As can be seen in Figure 12 the effect of the temperature on the effective neutron multiplication factor is essentially logarithmic.

Table 8. k_{eff} vs temperature with MCNP code for MYRRHA.

T (K)	k_{eff}
600	1.01660 ± 0.00003
900	1.01485 ± 0.00003
1200	1.01375 ± 0.00003
1500	1.01289 ± 0.00003
1800	1.01210 ± 0.00003
2100	1.01159 ± 0.00003
2400	1.01104 ± 0.00003
3000	1.01024 ± 0.00003

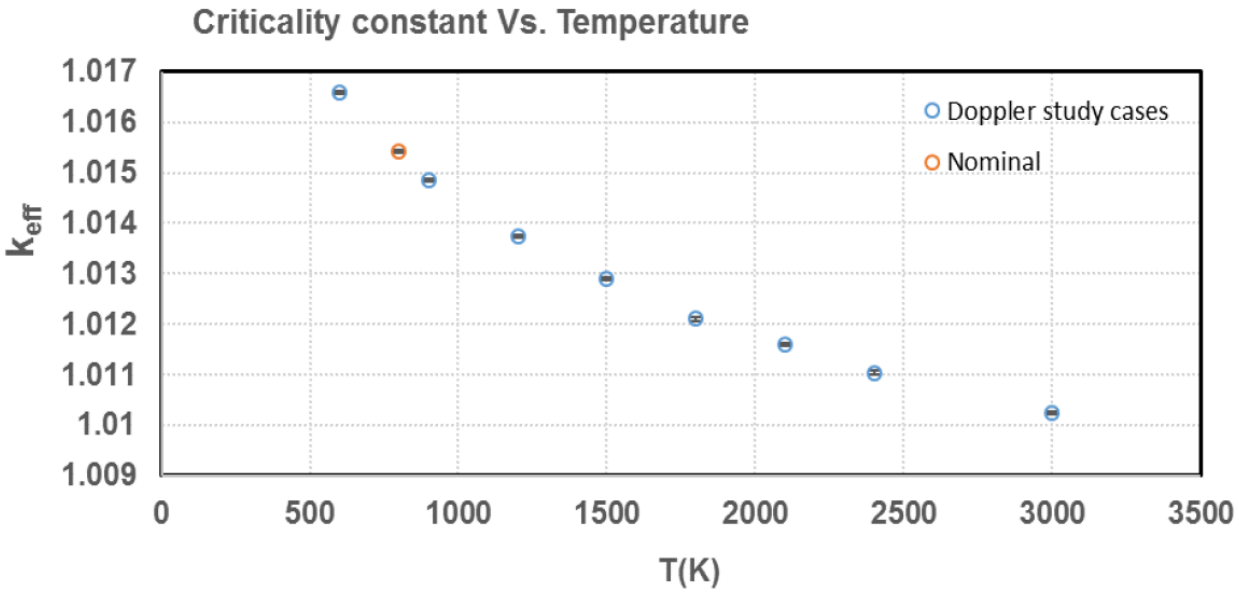

Figure 13. k_{eff} behavior with temperature.

The Doppler coefficient was calculated as the reactivity worth value divided by the temperature difference with the nominal case:

$$\rho_T = \frac{\Delta\rho}{T_{pert} - T_{nom}} \tag{8}$$

As can be seen in Figure 14, the effect on the reactivity is also, as expected, essentially logarithmic with respect to the temperature increase. The large uncertainties observed in some points of Figure 14 are due to the small difference between the perturbed and nominal case temperatures.

In Table 9, ISC for the major contributors to the uncertainty of the Doppler coefficient for 600 K only - corresponding to a decrease of 300 K with respect to fuel nominal temperature - are presented. ISC for all the temperatures requested in Table 8 are provided in Ref. [6]. Elastic scattering reactions of structural and coolant materials have a higher impact on the uncertainty, especially in lower temperature differences due to the significant statistical uncertainties on the same order of magnitude of the sensitivities. As temperature difference (and hence calculation precision) increases (n,f), ν_{Total} and ν_{Prompt} ^{239}Pu, ^{240}Pu and ^{238}U isotopes become dominant.

Differences between SCALE and SUMMON for a 300 K temperature decrease scenario for ALFRED (Table 3) and MYRRHA (Table 9), respectively, can be explained by the dominant effect of statistical uncertainties in SUMMON.

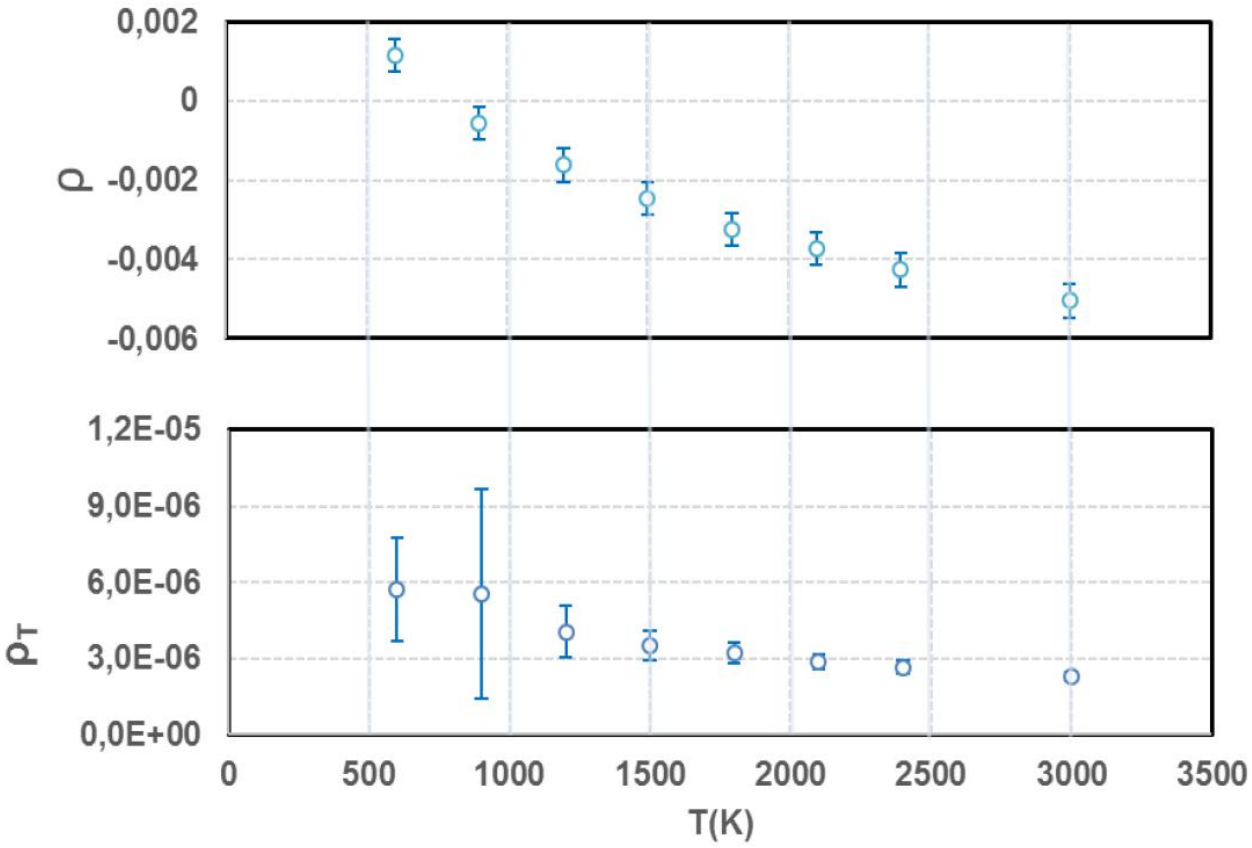

Figure 14. Reactivity and Doppler coefficient.

Table 9. ISC for the major contributions to the ρ uncertainty due to nuclear data in MYRRHA. ISC obtained with MCNP (JEFF-3.3) + SUMMON.

SUMMON - ρ_T					
T (K)	**Quantity**		*ISC* **(%/%)**		
600	^{16}O	el.	3.628E+00	±	1.777E+00
	^{56}Fe	el.	2.137E+00	±	1.808E+00
	^{209}Bi	el.	1.385E+00	±	2.272E+00
	^{208}Pb	el.	1.229E+00	±	1.605E+00
	^{239}Pu	(n,f)	-1.014E+00	±	5.404E-01
	^{56}Fe	(n,n')	-8.786E-01	±	3.048E-01
	^{206}Pb	el.	7.915E-01	±	9.603E-01
	^{239}Pu	el.	7.647E-01	±	7.765E-01
	^{239}Pu	$\bar{\upsilon}_p$	-6.252E-01	±	5.277E-01
	^{207}Pb	el.	5.499E-01	±	9.763E-01

4.2.4. Void

In Ref. [37], several voiding scenarios for MYRRHA are defined. In this work, voiding of the central IPS for a height of 18 cm calculated with SUMMON and a 100% voiding of the active region (height of 65 cm) calculated with Serpent 2 are presented. S/U analyses for all the voiding scenarios defined in Ref. [37] can be found in Ref. [6]. These particular scenarios have been chosen due to the different dominant physical effects in each of them, i.e., a hardening of the spectrum resulting in an increase of reactivity for the central IPS voiding scenario and increase of leakage resulting in a decrease of reactivity for the 100% voiding scenario. Void reactivity worth for both scenarios is shown in Table 10.

Table 10. Void reactivity worth for the selected scenarios for MYRRHA.

Voiding scenario	ρ_ρ (pcm)
Central IPS ± 9 cm	11 ± 4
100% in active region	-3070 ± 2

The ISC for the major contributions to the uncertainty of the void worth value in central IPS ± 9 cm scenario are shown in Table 11. It can be observed that the largest contributions are elastic reactions in elements of the fuel, coolant and structural materials, such as O, Cr, Fe, Bi, Pb, Pu and U. Relative uncertainties are notably high in this particular scenario, which is due to the small difference between the nominal and perturbed cases. For this reason, these results show very high uncertainties and the error in the contributions to the uncertainty of the individual reactions is largely consistent with zero.

Table 11. ISC for the major contributions to the ρ_ρ uncertainty in central IPS ± 9 cm void scenario in MYRRHA due to nuclear data. ISC obtained with MCNP (JEFF-3.3) + SUMMON.

SUMMON - ρ_ρ					
Scenario	**Quantity**		*ISC* **(%/%)**		
Central IPS ± 9 cm	^{16}O	el.	3.093E+01	±	2.061E+01
	^{208}Pb	el.	1.655E+01	±	1.748E+01
	^{209}Bi	el.	1.333E+01	±	2.604E+01
	^{56}Fe	el.	1.173E+01	±	2.087E+01
	^{240}Pu	el.	-9.123E+00	±	6.099E+00
	^{238}U	el.	-7.467E+00	±	6.425E+00
	^{54}Fe	el.	-7.424E+00	±	7.192E+00
	^{52}Cr	el.	-7.179E+00	±	8.480E+00
	^{206}Pb	el.	-6.867E+00	±	1.157E+01
	C-nat	el.	6.174E+00	±	4.151E+00

Top 10 ISC for the most important neutron induced nuclear data for MYRRHA 100% coolant voiding in the active region scenario are shown in Table 12. While statistical uncertainties are significant for this scenario too, a clear dominance of nubar, fission and capture reactions in Pu isotopes and ^{238}U is observed. Overall, scenarios analysed for ALFRED and MYRRHA differ in the spatial region and coolant density variation, resulting in a different ranking of reactions for the three of them (Table 4, Table 11 and Table 12). This is due to the underlying different physical effects in each of the scenarios, with spectral effects in the central IPS voiding scenario for MYRRHA, the beginning of the transition between spectral effects and leakage in the 20% voiding of the inner core region for ALFRED and the purely dominance of leakage in the 100% MYRRHA voiding scenario. In spite of the significant statistical uncertainties in some of the quantities, this is also reflected by the different integrated sensitivity coefficients, being positive in coolant and structural materials in the first, positive in coolant and negative in fuel in the second and being negative in fuel in the third.

Table 12. ρ_ρ ISC to the 10 most important neutron induced nuclear data for MYRRHA v 1.8 with JEFF-3.3 library and Serpent 2.

Serpent 2 - ρ_ρ					
Scenario	**Quantity**		*ISC* **(%/%)**		
100% void in active region	^{239}Pu	$\bar{\upsilon}_p$	-0.195	±	21.03%
	^{239}Pu	(n,f)	-0.382	±	15.70%
	^{238}U	(n,γ)	-0.233	±	13.94%
	^{241}Pu	$\bar{\upsilon}_p$	0.022	±	131.45%
	^{240}Pu	$\bar{\upsilon}_p$	-0.205	±	12.53%
	^{238}U	$\bar{\upsilon}_p$	-0.525	±	4.62%
	^{241}Pu	(n,f)	0.019	±	172.53%
	^{240}Pu	(n,f)	-0.166	±	17.41%
	^{239}Pu	(n,γ)	-0.044	±	48.49%
	^{238}U	(n,f)	-0.394	±	7.13%

4.2.5. Control rod insertion

The reactivity response due to the control rod insertion was calculated for two scenarios with SUMMON: in the first scenario, the buoyancy-driven control rods are fully inserted in the core while the gravity-safety control rods are fully out, in the second scenario both buoyancy-driven and gravity-safety control rods are fully inserted. In Table 13, integral control and safety rod worths are provided. As expected, the second scenario implies a higher reactivity response and a decrease of the criticality constant.

Table 13. Reactivity response due to control rods insertion. The first column presents the criticality constant and reactivity worth value of a scenario with only the buoyancy-driven (BD) control rods fully inserted; the second column also incorporates the gravity-safety (GS) control rods fully inserted.

MYRRHA - JEFF-3.3 - Control rods						
	BD			**BD+GS**		
k_{eff}	0.98824	±	0.00003	0.97461	±	0.00003
Δρ (pcms)	-2709	±	4	-4124	±	4

In Table 14, integrated sensitivity coefficients of the most important quantities for MYRRHA for buoyancy-driven and gravity-safety control rods insertion are presented. Reactions produced in the fuel material due to the shift in the neutron spectrum caused by the insertion of CR are key quantities in this reactivity response. The buoyancy-driven control rods in MYRRHA employ 90% ^{10}B-enriched boron carbide, B_4C as an absorbing material. Besides the availability of boron and the ease of its fabrication, the neutronic properties of the ^{10}B isotope are excellent even in the fast spectrum because of its (n,α) reaction cross section [44]. Thus, ^{10}B(n,α) is also a key quantity in this reactivity change scenario, with a strong negative contribution, as shown in Table 14.

Table 14. ISC for the major contributions to the ρ_{CR} uncertainty when the control rods are fully inserted due to nuclear data in MYRRHA. ISC obtained with MCNP (JEFF-3.3) + SUMMON.

SUMMON - ρ_{CR}					
Scenario	**Quantity**		*ISC* **(%/%)**		
Buoyancy driven control rods fully in	^{239}Pu	(n,f)	7.175E-01	±	2.395E-02
	^{10}B	(n,α)	-6.481E-01	±	1.990E-03
	^{239}Pu	$\bar{\upsilon}_p$	5.782E-01	±	2.373E-02
	^{238}U	(n,γ)	1.683E-01	±	3.119E-03
	^{208}Pb	el.	1.553E-01	±	6.427E-02
	^{238}U	$\bar{\upsilon}_p$	1.546E-01	±	5.158E-03
	^{240}Pu	$\bar{\upsilon}_p$	1.538E-01	±	3.782E-03
	^{240}Pu	(n,f)	1.361E-01	±	3.739E-03
Buoyancy driven and gravity safety	^{239}Pu	(n,f)	7.021E-01	±	1.500E-02
	^{10}B	(n,α)	-6.337E-01	±	1.399E-03
	^{239}Pu	$\bar{\upsilon}_p$	5.769E-01	±	1.484E-02
	^{238}U	$\bar{\upsilon}_p$	1.545E-01	±	3.324E-03
	^{238}U	(n,γ)	1.532E-01	±	2.179E-03
	^{240}Pu	$\bar{\upsilon}_p$	1.525E-01	±	2.585E-03
	^{240}Pu	(n,f)	1.353E-01	±	2.552E-03
	^{238}U	(n,f)	1.239E-01	±	3.480E-03

4.2.6. Power Peaking Factor

Sensitivity analysis of the PPF have been conducted with Serpent 2 code. Before showing the results for the sensitivity analysis, it is worth looking at Figure 15 which provides the power peaking map of each core assembly. As expected, the highest values are found in the innermost rings of the core, with the PPF decreasing with the distance from the core center. This implies that the inner zone has the highest number of fissions and therefore the highest power and temperature.

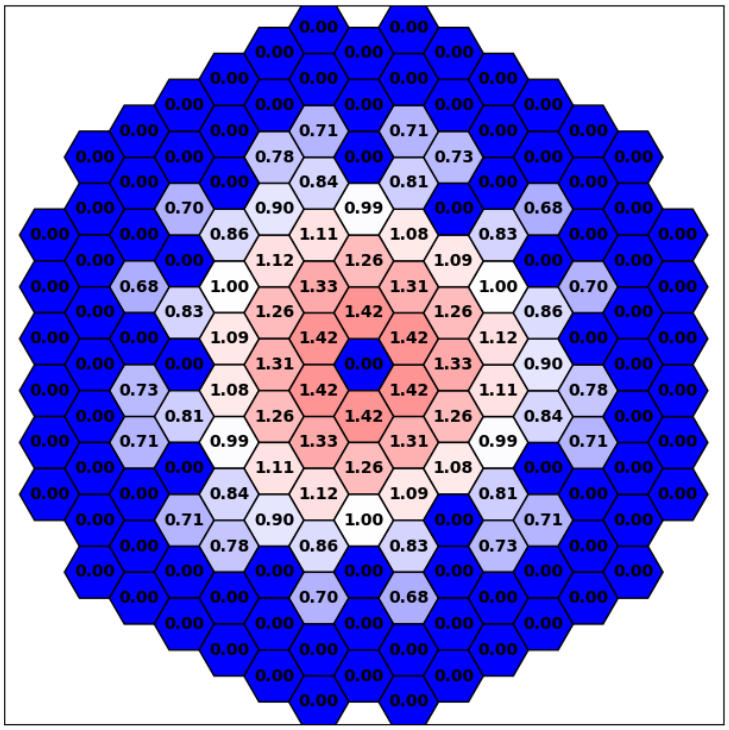

Figure 15. Power peaking map for MYRRHA v1.8 at Beginning of Life.

Since the PPF is the ratio of the assembly with the maximum power density to the average power density of the core, fission reactions in fuel isotopes are expected to be the quantities with highest sensitivity. As no reference to such a study has been found in the literature, the sensitivity coefficients resulting from a perturbation in the effective fission cross section have been determined for four important fissile isotopes: ^{238}U, ^{239}Pu, ^{240}Pu and ^{241}Pu.

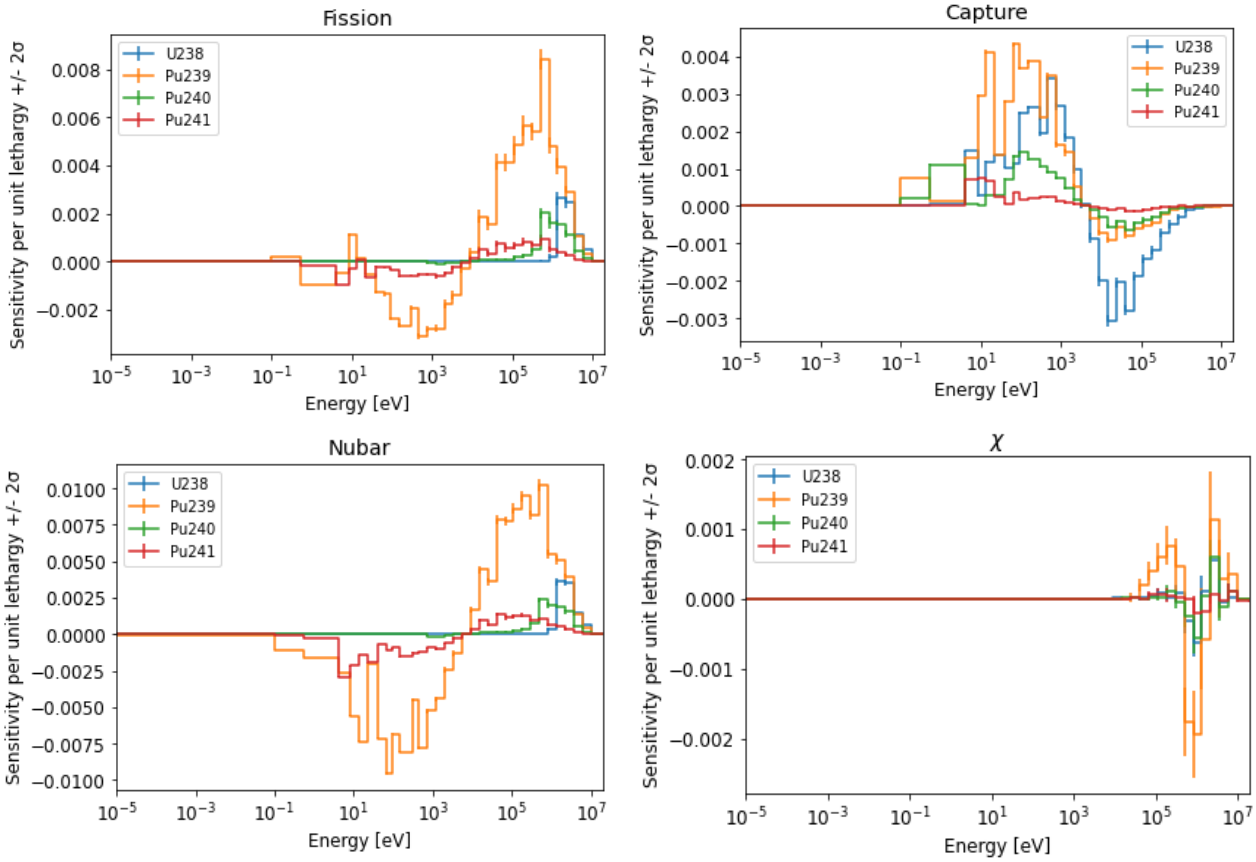

Figure 16. Energy dependent sensitivity of the power peaking factor in batch 101 of the core (Figure 7) for fission (upper left), capture (upper right), nubar (lower left) and chi (lower right) for ^{238}U, ^{239}Pu, ^{240}Pu and ^{241}Pu isotopes

The results of this analysis for the fission and capture cross sections and ν and χ in batch 101 of the core (see Figure 7) are presented in Figure 16. As expected, fission and capture show opposite behavior (when one is positive, the other is negative and vice versa), while nubar and fission present a similar behavior as they are closely related.

To understand the shape of each figure, it is useful to analyse the behavior of each case for each ring of the nucleus. The values obtained indicate how a perturbation in the neutron flux affects the value of the power peaking factor, so it is important to consider how the spectrum evolves with the distance from the central area of the core (see Figure 17).

Starting with fission (Figure 18), the first thing that stands out is that the results obtained for rings 1 and 2 are practically the same, since both are part of the inner core, where fission in the fast spectrum predominates. This explains the positive peak in the fast energy region. As expected, neutron capture shows the opposite behaviour, since where more fissions occur, captures are reduced and vice versa. If one looks at Figure 17, where the neutron fluxes of rings 1 and 5 have been plotted, the importance of the region of the core under analysis becomes clear. The first ring presents a threshold value below which one can assume that the spectrum becomes zero, while for the fifth ring, there is a thermal tail with significant resonances starting at energies of the order of eV. In fact, the shape of the spectrum in this ring closely resembles that of the spectrum obtained in the dummy assemnblies (see Ref. [5]).

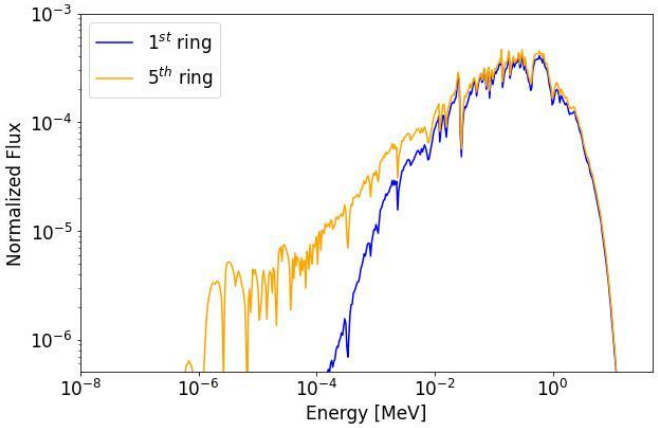

Figure 17. Neutron spectra in 1st and 5th rings for MYRRHA v1.8 at Beginning of Life.

The same analysis is valid to understand the remaining cases (Figure 19, Figure 20 and Figure 21), where, due to the similarity of the spectra in the first two rings, the sensitivity coefficients in both regions of the core are practically the same. The third ring behaves as a transition zone until the core region where the thermal spectrum becomes more prominent is reached.

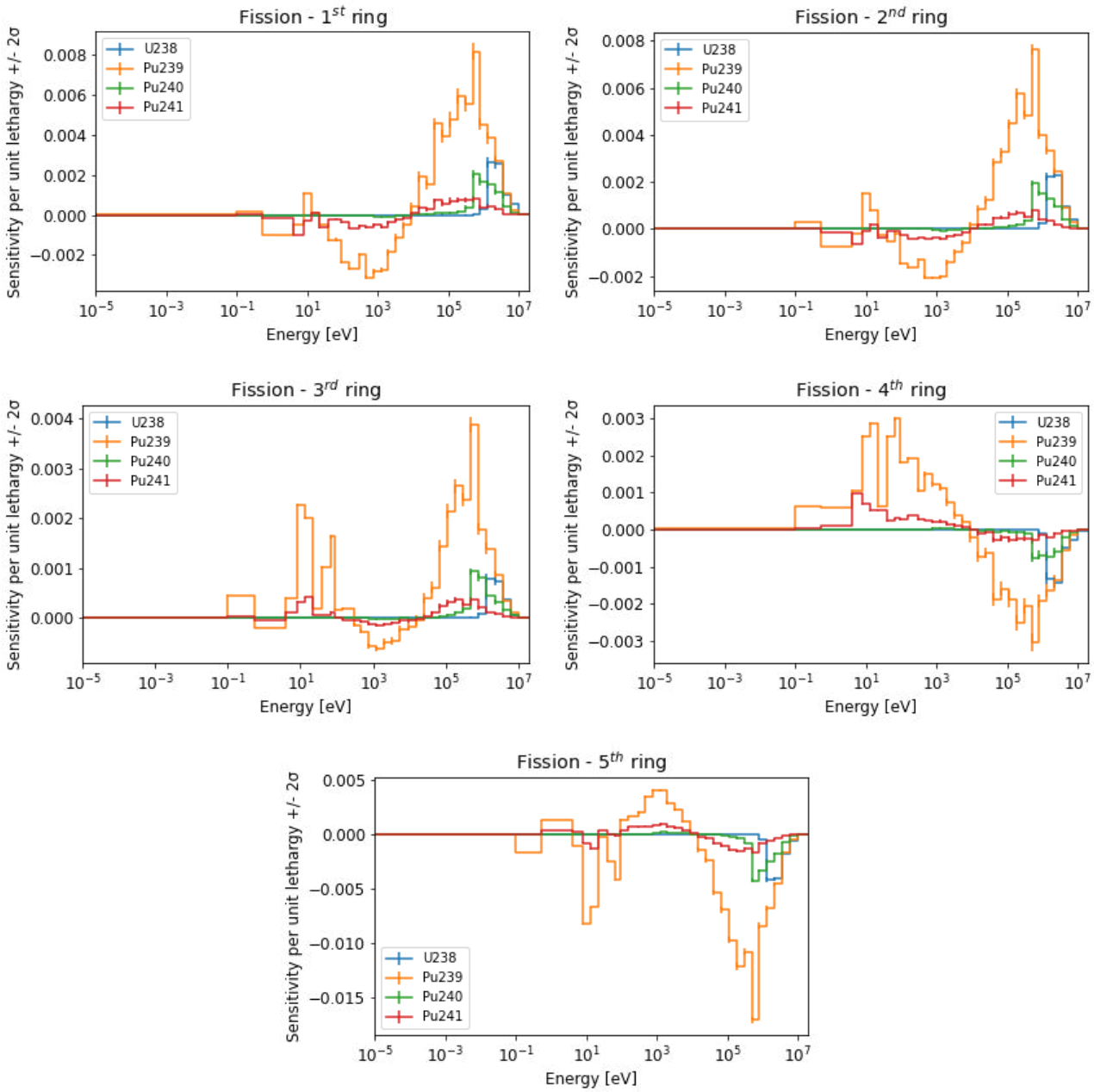

Figure 18. Energy dependent sensitivity coefficients of PPF in different fuel assembly rings for fission.

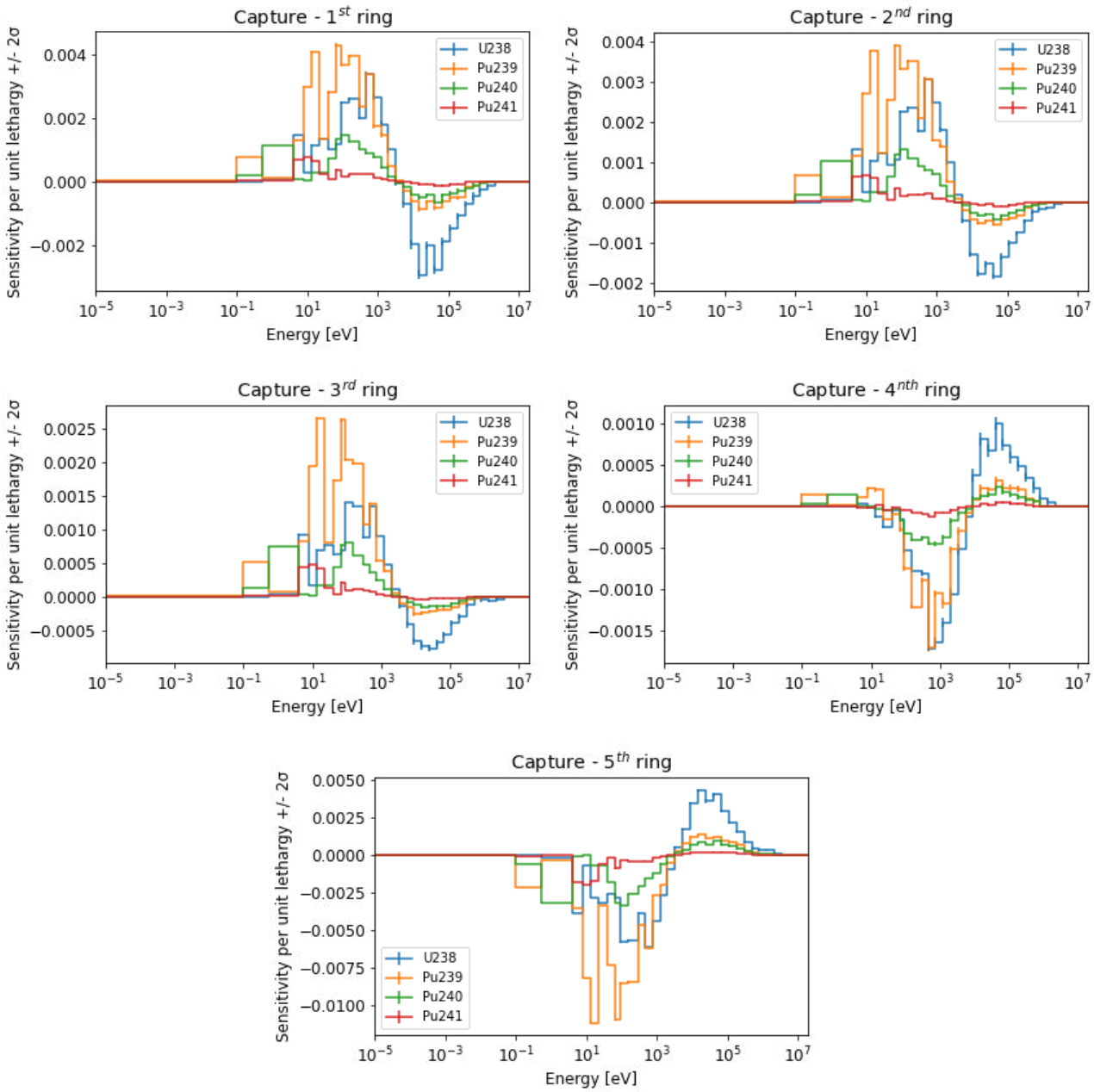

Figure 19. Energy dependent sensitivity coefficients of PPF in different fuel assembly rings for capture.

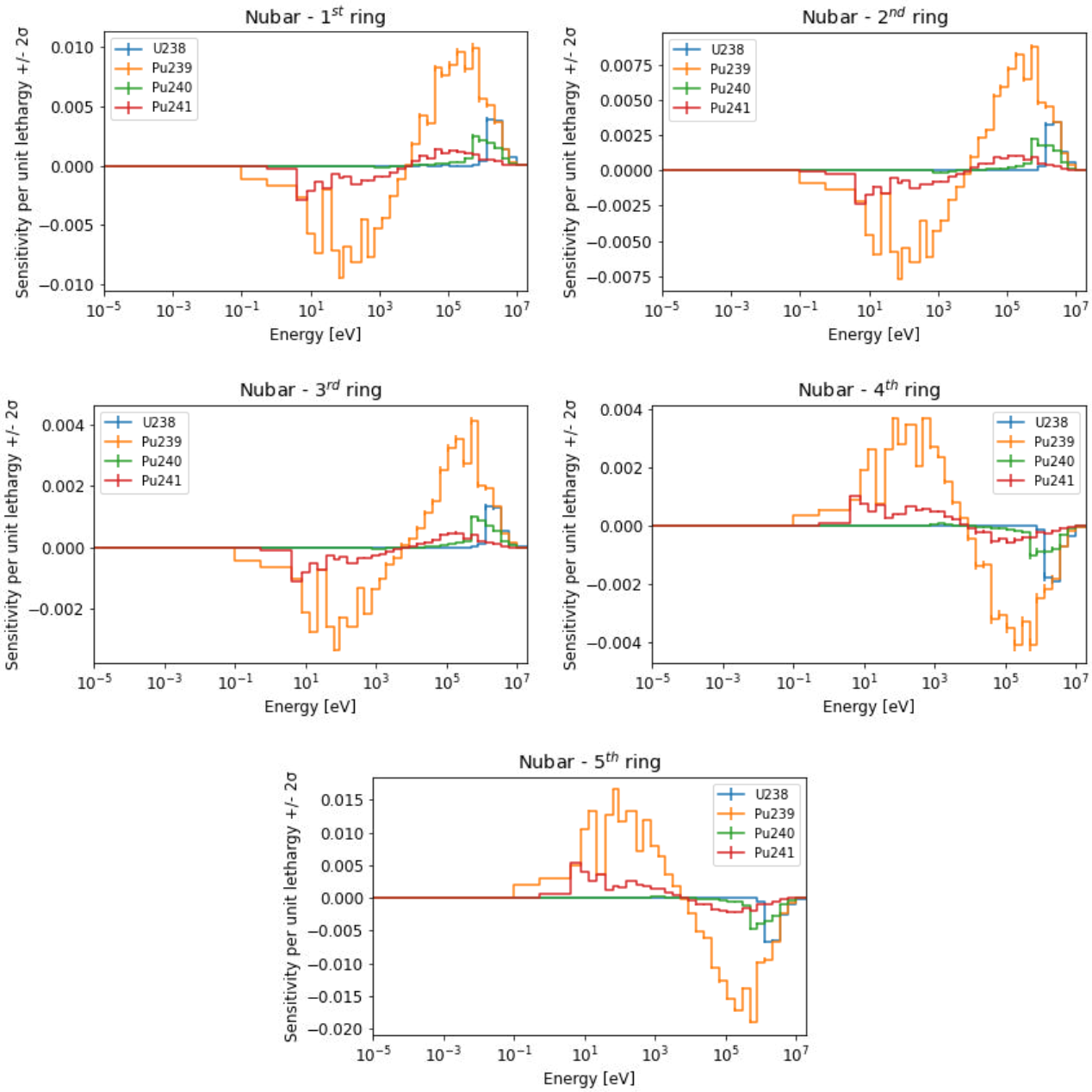

Figure 20. Energy dependent sensitivity coefficients of PPF in different fuel assembly rings for nubar.

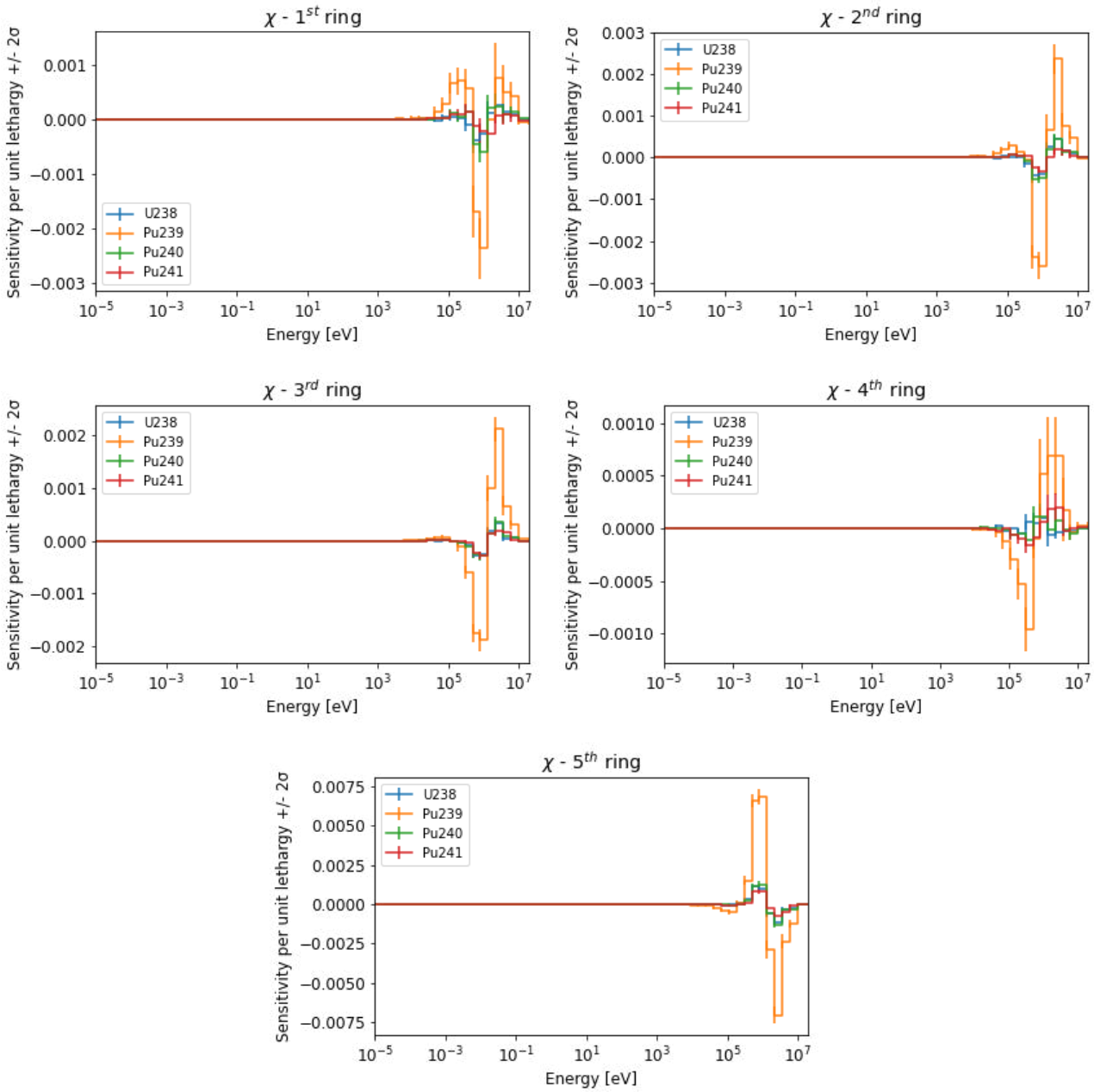

Figure 21. Energy dependent sensitivity coefficients of PPF in different fuel assembly rings for χ.

5. Uncertainty analysis

5.1. ESFR, ASTRID and ALFRED

Table 15 shows a summary of the uncertainty quantification analysis for the analysed reactor integral responses using JEFF-3.3 covariances in both 33 and 7 energy groups. Results with the state-of-the-art 56g ENDF/B-VIII.0 SCALE covariance matrix can be also found in Ref. [8]. The total uncertainties are compared to the design target accuracies for fast reactors recently updated by the OECD/NEA Working Party on International Nuclear Data Evaluation Co-operation (WPEC) Subgroup 46 [11]. The detailed breakdown of uncertainty contributors are shown in Table 16 - Table 19. The uncertainty values (in %) given in the tables have two different terms. The first term corresponds to the uncertainty due to nuclear data, and the second term (±) is the term corresponding to the stochastic calculation of sensitivity profiles.

Table 15. Summary of uncertainty quantification results for ESFR, ASTRID and ALFRED.

Reactor	Response	Target accuracy	Uncertainty [%] 33g Sensitivites 33g JEFF-3.3 COV			Uncertainty [%] 7g Sensitivites 7g JEFF-3.3 COV		
ESFR	**k-eff**	0.2% = 200 pcm	1.04	±	2.5E-04	0.98	±	4.5E-04
	Coolant density	5%	8.49	±	4.4E-02	9.14	±	5.5E-02
	Doppler+300K	5%	4.12	±	8.4E-01	3.65	±	7.2E-01
	Control	3%	1.85	±	1.9E+00	1.73	±	2.2E-02
ASTRID	**k-eff**	0.2%	0.97	±	2.0E-04	0.92	±	3.6E-04
	Coolant density	5%	15.78	±	5.2E-02	16.19	±	7.7E-02
ALFRED	**k-eff**	0.435% = 435 pcm	0.88	±	1.6E-04	0.84	±	3.0E-04
	Coolant density	5%	6.82	±	2.7E-01	6.42	±	3.6E-01
	Doppler+300K	5%	6.91	±	6.2E-01	6.55	±	7.8E-01
	Doppler-300K	5%	3.57	±	3.3E-01	3.46	±	4.8E-01

Table 16. Detailed breakdown of uncertainty contributors of k_{eff} (contributing more than ~200 pcm) for ESFR, ASTRID and ALFRED.

Covariance matrix: 7g JEFF-3.3 COV												
ESFR				**ASTRID**				**ALFRED**				
Quantity	**Δk/k (%)**		**Std. Dev.**	**Quantity**	**Δk/k (%)**		**Std. Dev.**	**Quantity**	**Δk/k (%)**		**Std. Dev.**
^{240}Pu (n,f)	0.57	±	1E-05	^{240}Pu (n,f)	0.50	±	1E-05	^{240}Pu (n,f)	0.55	±	2E-05
^{238}U (n,n')	0.47	±	3E-04	^{238}U (n,n')	0.39	±	2E-04	^{240}Pu (n,f) (n,γ)	-0.41	±	1E-05
^{240}Pu (n,f) (n,γ)	-0.41	±	9E-06	^{240}Pu (n,f) (n,γ)	-0.37	±	7E-06	^{239}Pu ν	0.32	±	1E-06
^{238}U (n,n') (n,f)	-0.34	±	1E-04	^{239}Pu (n,f)	0.34	±	8E-06	^{239}Pu (n,f)	0.32	±	7E-06
^{239}Pu (n,f)	0.33	±	6E-06	^{239}Pu ν	0.31	±	5E-07	^{238}U (n,n')	0.24	±	2E-04
^{239}Pu χ	0.32	±	1E-05	^{238}U (n,n') (n,f)	-0.30	±	8E-05	^{238}U (n,γ)	0.22	±	1E-05
^{238}U (n,n') (n,γ)	0.29	±	2E-04	^{239}Pu χ	0.30	±	8E-06	^{239}Pu χ	0.22	±	9E-06
^{239}Pu ν	0.29	±	6E-07	^{238}U (n,γ)	0.28	±	1E-05	^{238}U (n,n') (n,f)	-0.20	±	6E-05
^{238}U (n,γ)	0.29	±	2E-05	^{238}U (n,n') (n,γ)	0.26	±	2E-04	^{239}Pu (n,f) (n,γ)	0.19	±	5E-06
^{238}U (n,f)	0.20	±	6E-06	^{238}U (n,f)	0.19	±	5E-06	^{240}Pu (n,γ)	0.19	±	5E-06
^{238}U (n,f) (n,γ)	0.19	±	6E-06	^{238}U (n,f) (n,γ)	0.18	±	5E-06	^{238}U (n,n') (n,γ)	0.18	±	2E-04
TOTAL OF LISTED	0.90 (92% TOTAL)			TOTAL OF LISTED	0.83 (91% TOTAL)			TOTAL OF LISTED	0.75 (89% TOTAL)		
TOTAL	**0.98**	**±**	**4E-04**	**TOTAL**	**0.92**	**±**	**4E-04**	**TOTAL**	**0.84**	**±**	**3.0E-04**

Table 17. Detailed breakdown of uncertainty contributors of Doppler effect (top-5 contributors) for ESFR, ASTRID and ALFRED.

	Covariance matrix: 7g JEFF-3.3 COV								
	ESFR				ALFRED				
	Quantity	Δρ/ρ (%)		Std. Dev.	Quantity	Δρ/ρ (%)		Std. Dev.	
Doppler +300K	^{240}Pu (n,f)	1.86	±	1E-01	^{238}U (n,n')	4.20	±	7E-01	
	^{56}Fe el.	1.77	±	4E-01	^{238}U el. (n,n')	2.45	±	2E-01	
	^{239}Pu (n, γ)	0.92	±	7E-03	^{206}Pb (n,n')	2.12	±	1E-01	
	^{240}Pu (n,f) (n, γ)	0.88	±	2E-02	^{238}U (n,n') (n, γ)	1.76	±	9E-02	
	^{239}Pu (n,f)	0.79	±	2E-02	^{240}Pu (n,f)	1.56	±	7E-03	
	TOTAL OF LISTED				TOTAL OF LISTED	5.80 (89% TOTAL)			
	TOTAL				**TOTAL**	**6.55**	**±**	**8E-01**	
Doppler -300K					^{16}O el.	1.56	±	4E-01	
					^{240}Pu (n,f)	1.51	±	8E-03	
					^{239}Pu (n, γ)	1.32	±	8E-03	
					^{238}U (n,n')	1.24	±	2E-01	
					^{238}U el. (n,n')	1.20	±	1E-01	
					TOTAL OF LISTED	3.07 (89% TOTAL)			
					TOTAL	**3.46**	**±**	**5E-01**	

Table 18. Detailed breakdown of uncertainty contributors on coolant density effect (contributing more than ~2%) for ESFR, ASTRID and ALFRED.

Covariance matrix: 7g JEFF-3.3 COV												
ESFR				ASTRID				ALFRED				
Quantity	Δρ/ρ (%)		Std. Dev.	Quantity	Δρ/ρ (%)		Std. Dev.	Quantity	Δρ/ρ (%)		Std. Dev.	
^{239}Pu (n,f)	6.93	±	1E-02	^{239}Pu (n,f)	11.5	±	5E-03	^{206}Pb (n,n')	4.58	±	1E-01	
^{239}Pu (n,γ)	3.18	±	1E-03	^{239}Pu (n,γ)	6.34	±	3E-03	^{238}U (n,n')	3.18	±	2E-01	
^{238}U (n,n')	2.57	±	2E-02	^{238}U (n,n')	6.07	±	6E-02	^{207}Pb (n,n')	2.38	±	4E-02	
^{239}Pu (n,f) (n, γ)	2.43	±	1E-03	^{238}U (n,n') (n,f)	-4.46	±	2E-02	^{238}U (n,n') (n,f)	2.17	±	7E-02	
^{23}Na el.	2.36	±	2E-02	^{239}Pu (n,f) (n, γ)	-4.39	±	9E-04	^{238}U (n,n') (n,γ)	1.97	±	1E-01	
^{238}U (n,γ)	2.21	±	6E-04	^{238}U (n,γ)	3.75	±	1E-03	^{239}Pu (n,f)	1.54	±	4E-03	
^{241}Pu (n,f)	2.04	±	3E-03	^{23}Na (n,γ)	3.70	±	2E-04	^{208}Pb (n,n')	1.33	±	3E-02	
				^{240}Pu (n,f)	3.23	±	2E-03					
				^{56}Fe el.	3.10	±	4E-02					
				^{238}U el. (n,n')	-3.08	±	2E-02					
				^{241}Pu (n,f)	2.65	±	4E-04					
				^{238}U (n,f)	2.54	±	1E-03					
				^{240}Pu (n,f) (n, γ)	2.42	±	1E-03					
				^{238}U (n,f) (n, γ)	2.26	±	9E-04					
				^{238}U (n,n') (n,γ)	-2.18	±	2E-02					
				^{56}Fe (n,γ)	2.16	±	8E-04					
				^{23}Na (n,n')	2.09	±	1E-03					
				^{238}U el. (n,f)	2.02	±	9E-03					
				^{239}Pu χ	1.85	±	7E-04					
				^{23}Na el.	1.71	±	1E-02					
				TOTAL OF LISTED	15.71 (97% TOTAL)			TOTAL OF LISTED	5.69 (89% TOTAL)			
				TOTAL	16.19	**±**	**8E-02**	**TOTAL**	**6.42**	**±**	**4E-01**	

Table 19. Detailed breakdown of uncertainty contributors of control rod worth (top-5 contributors) ESFR.

Covariance matrix: 7g JEFF-3.3 COV			
ESFR			
Quantity	**Δρ/ρ (%)**		**Std. Dev.**
^{240}Pu (n,f)	1.14	±	6E-03
^{238}U (n,f)	0.52	±	1E-03
^{56}Fe el.	0.51	±	9E-03
^{238}U (n,n') (n,f)	0.51	±	4E-03
^{16}O el.	0.49	±	4E-03

The uncertainty analysis shows:

- The major contributors to k_{eff} uncertainties for the three reactors are the same actinides: ^{240}Pu, ^{239}Pu and ^{238}U. In order to meet the k_{eff} target accuracies for the three reactors, it is imperative to reduce the uncertainty in the reactions contributing with more than ~300 pcm:
    - ^{240}Pu (n,f)
    - ^{238}U (n,n') and ^{238}U (n,γ)
    - ^{239}Pu ν, ^{239}Pu (n,f) and ^{239}Pu χ
    - Good correlated data between fission and capture of ^{240}Pu, ^{240}Pu (n,f) (n,γ), as well as between fission and inelastic of ^{238}U, ^{238}U (n,f) (n,n'), are needed because of the significant impact of the energy correlation of those cross-sections on the uncertainty estimation.
- The major contributors to Doppler uncertainties differ significantly between SFR and LFR. The uncertainty in the Doppler effect for LFR following a temperature increase exceeds the target accuracy (assuming it is 5%) while the accuracy is not exceeded following a temperature decrease. The main contributor is ^{238}U (n,n'), which is responsible of 64% of the global uncertainty in the parameter, followed by the covariance terms ^{238}U el.(n,n') and ^{238}U (n, γ)(n,n') and by ^{206}Pb (n,n'). Since sensitivity of Doppler effect to ^{238}U (n,n') is less important in SFR, its contribution to Doppler uncertainty is not so relevant. In summary, Doppler S/U analysis leads to include the following cross-sections contributing to uncertainty more than ~2% in the potential list for uncertainty reduction:
    - ^{206}Pb (n,n')
    - Correlated data ^{238}U el. (n,n') and ^{238}U (n,n') (n, γ)
- The uncertainty in sodium voiding for SFR by far exceeds the target accuracy (assuming it is 5%). Main contributors are ^{239}Pu (fission and capture) and ^{238}U cross sections. Fission of ^{240}Pu and ^{241}Pu also play a role. Regarding non-actinide isotopes, ^{56}Fe contributes via capture and elastic scattering and ^{23}Na mainly via capture. Inelastic and elastic scattering of ^{23}Na are ranked as low as 17th and 20th respectively.

  It is worth it to mention that those conclusions correspond to a full voiding. The partial-voiding analysis performed for ASTRID-like reactor in Annex 3 of Ref. [8] shows that target accuracies are also exceeded when voiding only inner or outer fissile regions, while the lowest uncertainties correspond to the plenum voiding. The relative importance of major contributors changes among the different scenarios: when voiding plenum regions, elastic scattering of ^{56}Fe and ^{23}Na are the most important contributors; when voiding fuel regions, particularly the outer fuel zone, inelastic scattering of ^{23}Na becomes more relevant.
- The uncertainty in the cooling density effect for LFR exceeds the target accuracy (assuming it is 5%) mainly due to inelastic scattering of ^{206}Pb, ^{207}Pb and ^{238}U. However, in case of coolant density reduction in the outer zone, the contributor's importance changes, similarly to ASTRID.

  To cover all the possible scenarios, coolant density analysis leads to include the following cross-sections, contributing to uncertainty more than ~2%, in the potential list for uncertainty reduction:
    - ^{239}Pu (n,γ) and good correlated data with fission: ^{239}Pu (n, γ) (n,f)

- ^{238}U (n,f) and good correlated data with capture and elastic: ^{238}U (n,f) (n, γ) and ^{238}U el. (n,f)
- ^{23}Na (n,γ), elastic and inelastic
- ^{26}Fe elastic and (n, γ)
- Inelastic scattering of lead isotopes, ^{206}Pb, ^{207}Pb, ^{208}Pb

- The uncertainty in the control rod worth does not exceed the target accuracy (assuming it is 5%), so no additional uncertainty reduction would be required.
- Scattering reactions play a very relevant role in most examined reactivity effects. There is a significant sensitivity to the angular distribution of the neutrons scattered in these fast spectrum systems (especially after sodium voiding, as shown in Annex 2 of Ref. [8] for the ASTRID-like reactor). However, the impact of the covariances in the angular distribution of scattering data has not been considered, which could significantly affect uncertainty results, as shown in [45, 46]. Consequently, an identified gap in this study is the lack of consideration of covariances in angular scattering distributions.

5.2. MYRRHA

As mentioned in Section 2.2, uncertainty quantification analyses have been performed using the sensitivity coefficients from Serpent 2 and propagating the uncertainties in nuclear data to the uncertainty in the response using NDaST . However, the uncertainty quantification is limited since only sensitivities for the top 10 major quantities have been derived for each response with Serpent and uncertainties in ν and χ couldn't be propagated with NDaST. On the other hand complete uncertainty quantification analyses have been performed with SUMMON including all isotopes present in the model and all reaction channels. Therefore results derived with NDaST have not been included in this report but can be found in Ref. [7].

Results from the uncertainty quantification performed with SUMMON for reactivity responses analysed in Section 4.2, using the sensitivities calculated with SUMMON, are presented in Table 20 - Table 25. The total contribution to the uncertainty has been calculated including all reactions and not only the ones that are listed.

Table 20. Major contributors to the uncertainty in k_{eff} of MYRRHA with SUMMON and JEFF-3.3 library.

MYRRHA - JEFF-3.3						
Quantity				**k_{eff} uncertainty (%)**		
^{240}Pu	(n,f)	^{240}Pu	(n,f)	5.54E-01	±	6.61E-04
^{240}Pu	(n,f)	^{240}Pu	(n,γ)	-4.32E-01	±	1.72E-04
^{239}Pu	$\bar{\upsilon}_p$	^{239}Pu	$\bar{\upsilon}_p$	3.15E-01	±	2.03E-04
^{239}Pu	(n,f)	^{239}Pu	(n,f)	2.77E-01	±	3.20E-04
^{239}Pu	χ	^{239}Pu	χ	2.37E-01	±	2.88E-03
^{240}Pu	(n,γ)	^{240}Pu	(n,γ)	2.01E-01	±	8.37E-05
^{239}Pu	(n,f)	^{239}Pu	(n,γ)	1.82E-01	±	1.13E-04
^{238}U	(n,γ)	^{238}U	(n,γ)	1.72E-01	±	6.81E-05
^{238}U	(n,n')	^{238}U	(n,f)	-1.40E-01	±	3.66E-04
^{238}U	(n,n')	^{238}U	(n,n')	1.32E-01	±	3.24E-03
^{239}Pu	(n,γ)	^{239}Pu	(n,γ)	1.27E-01	±	1.74E-04
^{238}U	(n,f)	^{238}U	(n,γ)	1.21E-01	±	7.30E-05
^{238}U	(n,f)	^{238}U	(n,f)	1.14E-01	±	2.89E-04
^{238}U	(n,n')	^{238}U	(n,γ)	9.62E-02	±	1.81E-04
^{241}Pu	χ	^{241}Pu	χ	8.50E-02	±	1.20E-03
^{208}Pb	el.	^{208}Pb	el.	8.24E-02	±	4.08E-03
^{56}Fe	(n,γ)	^{56}Fe	(n,γ)	7.71E-02	±	1.57E-04
^{241}Pu	$\bar{\upsilon}$	^{241}Pu	$\bar{\upsilon}_p$	7.57E-02	±	5.63E-05
^{56}Fe	el.	^{56}Fe	el.	7.16E-02	±	3.55E-03
^{238}Pu	$\bar{\upsilon}$	^{238}Pu	$\bar{\upsilon}_p$	7.13E-02	±	5.07E-05
k_{eff} total uncertainty (%) =				7.62E-01	±	1.26E-03

Table 21. Major contributors to the uncertainty in β_{eff} of MYRRHA with SUMMON and JEFF-3.3 library.

MYRRHA - JEFF-3.3						
Quantity				β_{eff} uncertainty (%)		
^{241}Pu	$\bar{\upsilon}_d$	^{241}Pu	$\bar{\upsilon}_d$	6.99E-01	±	1.06E-03
^{239}Pu	χ	^{239}Pu	χ	6.16E-01	±	6.07E-02
^{238}U	(n,f)	^{238}U	(n,f)	4.71E-01	±	6.74E-03
^{238}U	(n,n')	^{238}U	(n,f)	-3.92E-01	±	5.91E-03
^{241}Pu	χ	^{241}Pu	χ	3.62E-01	±	2.50E-02
^{238}U	el.	^{238}U	(n,f)	3.22E-01	±	4.67E-03
^{240}Pu	(n,f)	^{240}Pu	(n,f)	2.80E-01	±	1.44E-02
^{239}Pu	$\bar{\upsilon}_p$	^{239}Pu	$\bar{\upsilon}_p$	2.64E-01	±	4.48E-03
^{238}U	(n,n')	^{238}U	(n,n')	2.59E-01	±	7.62E-02
^{238}U	el.	^{238}U	(n,n')	-2.44E-01	±	6.91E-02
^{56}Fe	el.	^{56}Fe	el.	1.51E-01	±	1.06E-01
^{57}Fe	el.	^{57}Fe	el.	1.43E-01	±	5.64E-02
^{238}U	(n,n')	^{238}U	(n,γ)	1.40E-01	±	6.35E-03
^{238}U	χ	^{238}U	χ	1.38E-01	±	1.45E-02
^{241}Pu	el.	^{241}Pu	el.	1.31E-01	±	8.48E-02
^{238}U	el.	^{238}U	el.	1.26E-01	±	6.49E-02
^{238}U	$\bar{\upsilon}_p$	^{238}U	$\bar{\upsilon}_p$	1.26E-01	±	1.97E-03
^{54}Fe	el.	^{54}Fe	el.	1.14E-01	±	5.07E-02
^{238}Pu	$\bar{\upsilon}_d$	^{238}Pu	$\bar{\upsilon}_d$	1.12E-01	±	1.59E-04
^{209}Bi	(n,n')	^{209}Bi	(n,n')	9.67E-02	±	1.70E-02
β_{eff} total uncertainty (%) =				1.26E+00	±	3.68E-02

Table 22. Major contributors to the uncertainty in ρ_T (T = 600 K) of MYRRHA with SUMMON and JEFF-3.3 library.

MYRRHA - JEFF-3.3						
Quantity				ρ_T uncertainty (%)		
^{57}Fe	el.	^{57}Fe	el.	7.84E+00	±	3.27E+00
^{16}O	el.	^{16}O	el.	7.16E+00	±	3.49E+00
^{56}Fe	el.	^{56}Fe	el.	6.70E+00	±	3.36E+00
^{58}Ni	el.	^{58}Ni	el.	4.59E+00	±	1.54E+00
^{54}Fe	el.	^{54}Fe	el.	4.16E+00	±	1.55E+00
^{60}Ni	el.	^{60}Ni	el.	4.07E+00	±	2.03E+00
^{238}U	el.	^{238}U	el.	3.91E+00	±	3.44E+00
^{58}Fe	el.	^{58}Fe	el.	3.12E+00	±	1.11E+00
^{208}Pb	el.	^{208}Pb	el.	3.09E+00	±	3.09E+00
^{241}Pu	(n,n')	^{241}Pu	(n,n')	3.08E+00	±	1.37E+00
^{240}Pu	(n,n')	^{240}Pu	(n,n')	2.93E+00	±	2.34E+00
^{240}Pu	el.	^{240}Pu	(n,n')	-2.90E+00	±	2.23E+00
^{56}Fe	(n,n')	^{56}Fe	(n,n')	2.85E+00	±	8.01E-01
^{206}Pb	el.	^{206}Pb	el.	2.57E+00	±	9.84E-01
^{238}U	el.	^{238}U	(n,n')	2.43E+00	±	1.10E+01
^{62}Ni	el.	^{62}Ni	el.	2.39E+00	±	1.63E+00
^{207}Pb	el.	^{207}Pb	el.	2.09E+00	±	7.76E-01
^{206}Pb	(n,n')	^{206}Pb	(n,n')	2.02E+00	±	1.51E+00
^{238}U	(n,n')	^{238}U	(n,n')	1.94E+00	±	3.40E+00
^{240}Pu	(n,f)	^{240}Pu	(n,f)	1.85E+00	±	8.12E-01
ρ_T total uncertainty (%) =				1.83E+01	±	3.22E-02

Table 23. Major contributors to the uncertainty in ρ_ρ (central IPS ± 9 cm void) of MYRRHA with SUMMON and JEFF-3.3 library.

MYRRHA - JEFF-3.3						
Quantity				**ρ_ρ uncertainty (%)**		
^{56}Fe	el.	^{56}Fe	el.	8.97E+01	±	5.11E+01
^{57}Fe	el.	^{57}Fe	el.	7.39E+01	±	3.66E+01
^{238}U	(n,n')	^{238}U	(n,n')	6.01E+01	±	3.93E+01
^{16}O	el.	^{16}O	el.	5.96E+01	±	4.05E+01
^{54}Fe	el.	^{54}Fe	el.	5.50E+01	±	3.46E+01
^{58}Ni	el.	^{58}Ni	el.	4.22E+01	±	2.04E+01
^{238}U	el.	^{238}U	(n,n')	-3.93E+01	±	3.28E+01
^{208}Pb	el.	^{208}Pb	el.	3.63E+01	±	3.61E+01
^{55}Mn	el.	^{55}Mn	el.	3.25E+01	±	2.97E+01
^{62}Ni	el.	^{62}Ni	el.	2.99E+01	±	1.88E+01
^{240}Pu	el.	^{240}Pu	el.	2.77E+01	±	1.97E+01
^{206}Pb	(n,n')	^{206}Pb	(n,n')	2.44E+01	±	2.12E+01
^{240}Pu	el.	^{240}Pu	(n,n')	-2.27E+01	±	5.82E+01
^{238}U	χ	^{238}U	χ	2.08E+01	±	8.62E+00
^{241}Pu	(n,n')	^{241}Pu	(n,n')	2.04E+01	±	1.09E+01
^{58}Fe	el.	^{58}Fe	el.	1.97E+01	±	1.16E+01
^{24}Mg	el.	^{24}Mg	el.	1.91E+01	±	2.21E+01
^{206}Pb	el.	^{206}Pb	el.	1.84E+01	±	7.62E+00
^{238}U	(n,n')	^{238}U	(n,f)	-1.83E+01	±	1.83E+01
^{238}U	el.	^{238}U	el.	1.70E+01	±	3.63E+01
ρ_ρ total uncertainty (%) =				1.82E+02	±	3.74E+01

Table 24. Major contributors to the uncertainty in ρ_{CR} (buoyancy-driven CR fully in) of MYRRHA with SUMMON and JEFF-3.3 library.

MYRRHA - JEFF-3.3						
Quantity				**ρ_{CR} uncertainty (%)**		
^{240}Pu	(n,f)	^{240}Pu	(n,f)	1.21E+00	±	3.51E-02
^{239}Pu	χ	^{239}Pu	χ	7.62E-01	±	1.50E-01
^{56}Fe	el.	^{56}Fe	el.	6.46E-01	±	1.61E-01
^{238}U	(n,n')	^{238}U	(n,n')	5.60E-01	±	1.90E-02
^{239}Pu	(n,f)	^{239}Pu	(n,f)	-5.29E-01	±	2.65E-02
^{238}U	(n,n')	^{238}U	(n,f)	5.19E-01	±	1.64E-02
^{240}Pu	(n,f)	^{240}Pu	(n,γ)	4.72E-01	±	1.24E-02
^{239}Pu	(n,γ)	^{239}Pu	(n,γ)	4.54E-01	±	1.92E-01
^{238}U	(n,n')	^{238}U	(n,γ)	-4.01E-01	±	1.06E-02
^{240}Pu	(n,n')	^{240}Pu	(n,f)	-3.89E-01	±	1.14E-02
^{239}Pu	(n,f)	^{239}Pu	(n,γ)	-3.29E-01	±	5.93E-03
^{238}U	el.	^{238}U	(n,n')	-3.26E-01	±	7.56E-02
^{238}U	(n,f)	^{238}U	(n,f)	3.21E-01	±	1.57E-02
^{241}Pu	el.	^{241}Pu	el.	3.04E-01	±	1.85E-01
^{208}Pb	el.	^{208}Pb	el.	2.96E-01	±	1.75E-01
^{238}U	(n,γ)	^{238}U	(n,γ)	2.71E-01	±	4.80E-03
^{57}Fe	el.	^{57}Fe	el.	2.57E-01	±	1.10E-02
^{239}Pu	$\bar{\upsilon}_p$	^{239}Pu	$\bar{\upsilon}_p$	2.53E-01	±	6.01E-02
^{241}Pu	χ	^{241}Pu	χ	2.40E-01	±	1.15E-01
^{238}U	el.	^{238}U	(n,f)	2.35E-01	±	1.16E-02
ρ_{CR} total uncertainty (%) =				1.96E+00	±	9.99E-02

Table 25. Major contributors to the uncertainty in ρ_{CR} (buoyancy-driven CR and gravity SR fully in) of MYRRHA with SUMMON and JEFF-3.3 library.

MYRRHA - JEFF-3.3						
Quantity				**ρ_{CR} uncertainty (%)**		
^{240}Pu	(n,f)	^{240}Pu	(n,f)	1.21E+00	±	2.24E-02
^{239}Pu	χ	^{239}Pu	χ	7.12E-01	±	9.95E-02
^{238}U	(n,n')	^{238}U	(n,n')	6.67E-01	±	1.18E-01
^{239}Pu	(n,f)	^{239}Pu	(n,f)	5.62E-01	±	1.21E-02
^{238}U	(n,n')	^{238}U	(n,f)	-5.24E-01	±	1.76E-02
^{240}Pu	(n,f)	^{240}Pu	(n,γ)	4.98E-01	±	1.10E-02
^{238}U	(n,n')	^{238}U	(n,γ)	-4.18E-01	±	7.84E-03
^{239}Pu	(n,γ)	^{239}Pu	(n,γ)	4.16E-01	±	8.00E-03
^{56}Fe	el.	^{56}Fe	el.	3.95E-01	±	1.36E-01
^{238}U	el.	^{238}U	(n,n')	-3.81E-01	±	6.47E-02
^{238}U	(n,f)	^{238}U	(n,f)	3.19E-01	±	1.05E-02
^{239}Pu	(n,f)	^{239}Pu	(n,γ)	-3.18E-01	±	4.17E-03
^{238}U	el.	^{238}U	(n,f)	2.75E-01	±	9.11E-03
^{239}Pu	$\bar{\upsilon}_p$	^{239}Pu	$\bar{\upsilon}_p$	2.56E-01	±	6.90E-03
^{238}U	(n,γ)	^{238}U	(n,γ)	2.47E-01	±	3.37E-03
^{10}B	(n,α)	^{10}B	(n,α)	2.13E-01	±	4.72E-04
^{241}Pu	χ	^{241}Pu	χ	2.10E-01	±	3.89E-02
^{16}O	el.	^{16}O	el.	1.91E-01	±	9.78E-02
^{240}Pu	(n,n')	^{240}Pu	(n,f)	-1.88E-01	±	4.12E-03
^{57}Fe	el.	^{57}Fe	el.	1.82E-01	±	5.40E-02
ρ_{CR} total uncertainty (%) =				1.85E+00	±	6.12E-02

The uncertainty in k_{eff} due to nuclear data is 0.76%. The main contributions to the uncertainty of the k_{eff} are fission and capture reactions in plutonium isotopes ^{239}Pu and ^{240}Pu. There are also noticeable contributions of the inelastic reaction of ^{238}U and inelastic reactions of ^{208}Pb and ^{56}Fe. Good agreement is obtained with results derived with NDaST in Ref. [7]. Good agreement is also obtained with ALFRED.

The delayed fission ν and other fission-related data have the highest impact on the total uncertainty in β_{eff}. In any case, it is important to remark, again that the JEFF-3.3 library does not contain covariance matrices for the delayed fission ν of relevant isotopes (^{239}Pu, ^{240}Pu, ^{238}U), and this uncertainty is underestimated. In Ref. [30], uncertainty quantification for MYRRHA is performed with JENDL-4.0 nuclear data library [47] which contains covariances for these quantities. An uncertainty ~2.3% is obtained.

The main contributors for the uncertainty due to a decrease of 300 K in fuel temperature (Doppler) are the elastic and inelastic reactions in elements of the structural materials, coolant and fuel such as O, Mg, Mn, Fe, Ni, Pb, U and Pu. With the temperature increase in the fuel materials (Ref. [6]), fission reactions also gain importance in the contribution to the uncertainty, although scattering reactions remain dominant. The large statistical uncertainty, however, does not allow being conclusive about it, which also explains differences with ALFRED.

Regarding the uncertainty in the central IPS ± 9 cm voiding scenario, it can be observed that the largest contributions are elastic and inelastic reactions in elements of the fuel, coolant and structural materials, such as O, Mn, Fe, Ni, Pb, U and Pu. When the void height starts to increase (Ref. [6]), it also emerges as noticeable the impact of the total fission χ in the isotopes ^{239}Pu and ^{241}Pu. As mentioned above, relative uncertainties are notably high in this particular scenario, which is due to the small difference between the nominal and perturbed cases. For this reason, these results show very high uncertainties and the error in the contributions to the uncertainty of the individual reactions is largely consistent with zero, at least for the two lower void heights.

^{240}Pu fissions are the main contributors to the uncertainty in control rod worth, as it was the case of k_{eff}, although the highest sensitivity was to ^{239}Pu fissions. These results are very similar in the second scenario when safety control rods are also fully inserted.

6. Conclusions

S/U analysis have been performed for the ESFR, ASTRID and ALFRED advanced reactor systems and the multi-purpose flexible irradiation facility MYRRHA, with SCALE, Serpent 2 and SUMMON codes and JEFF-3.3 nuclear data library for relevant reactor safety parameters, namely k_{eff}, β_{eff}, Doppler reactivity coefficients, void worth, reactivity worth of control rods and power peaking factor (MYRRHA).

A ranking of the most important isotopes and reactions for each parameter has been derived for all the systems. Uncertainties have been quantified and have been found to be higher than target accuracies proposed. Therefore, recommendations of nuclear data in need of improvement have been given. It should be noted that all reactors analysed employ MOX fuel and that some of the reactivity effects, such as the Doppler coefficient, have a strong sensitivity to reactions in the fuel. Thus, results can vary for SFRs and LFRs employing other type of fuel, such as Heavy Enriched Uranium.

An identified gap in this work is the lack of consideration of covariances in angular scattering distributions. Due to the importance of scattering reactions in most examined reactivity effects, that aspect should receive more attention, together with the large statistical deviations accompanying scattering reaction sensitivities.

As a result of this work, recommendations to the JEFF project will be given in T5.2 and deliverable D5.5. They will be communicated to the JEFF community for consideration in the next release of the JEFF nuclear data library, JEFF-4, planned for 2024.

Acknowledgements

The research leading to these results has received funding from the Euratom research and training programme 2014-2018 under Grant Grant Agreement Number 847552 (SANDA Project). This work has been also supported by the ENRESA-CIEMAT agreement "Trasmutación de Radionucleidos de Vida Larga como Soporte a la Gestión de Residuos Radiactivos de Alta Actividad".

The ESFR model has been obtained through the HORIZON2020 EU ESFR-SMART project (number 754501), while ASTRID-like and ALFRED models through the 7th FP EU ESNII plus project (number 605172).

SCALE6.3 beta version has been provided by Oak Ridge National Laboratory. MCNP 6.2 has been obtained through RSICC.

References

[1] EC Community Research and Development Information Service. SANDA - Supplying Accurate Nuclear Data for energy and non-energy Applications. https://cordis.europa.eu/project/id/847552. 2022.

[2] Plompen AJM. Status of the JEFF-3.3 paper and JEFF-4.0. OECD/NEA JEFDOC-1974. 2019.

[3] EC Community Research and Development Information Service. ESNII PLUS - Preparing ESNII for HORIZON 2020. https://cordis.europa.eu/project/id/605172. 2022.

[4] EC Community Research and Development Information Service. ESFR-SMART - European Sodium Fast Reactor Safety Measures Assessment and Research Tools. https://cordis.europa.eu/project/id/754501. 2022.

[5] Fiorito L, Hernandez-Solis A, Romojaro P. Homogenized neutronics model of MYRRHA design revision 1.8. SCK CEN Report SCK CEN/44767116. 2021.

[6] Panizo S, Bécares V. Report on S/U analyses in MYRRHA homogenized model v1.8 performed with the MCNP6.2 and SUMMON codes and the JEFF-3.3 library. CIEMAT Report DFN/IN-03/II-22, issued on 19 October 2022. 2022.

[7] Alfonso C. Target Accuracy Requirements for MYRRHA. UPM MSc. Thesis. 2022.

[8] García-Herranz N, Jiménez-Carrascosa A, Cabellos O. UPM contribution to D5.2: Report on ESFR, ASTRID and ALFRED sensitivity and impact studies. UPM Report. 2022.

[9] Wieselquist WA, Lefebvre RA, Jesse MA. SCALE Code System. Oak Ridge National Laboratory Report ORNL/TM-2005/39, Version 6.2.4. 2020.

[10] Leppänen J, Pusa M, Viitanen T, Valtavirta V, Kaltiaisenaho T. The Serpent Monte Carlo code: Status, development and applications in 2013. Annals of Nuclear Energy. 2015;82:142-50.

[11] Salvatores M. Introduction to TAR. OECD/NEA WPEC SG46. 2019.

[12] Plompen AJM, Cabellos O, De Saint Jean C, Fleming M, Algora A, Angelone M, et al. The joint evaluated fission and fusion nuclear data library, JEFF-3.3. Eur Phys J A. 2020;56:181.

[13] Wiarda D, Dunn ME, Greene NM, Williams ML, Celik C, Petrie LM. AMPX-6: A Modular Code System for Processing ENDF/B. Oak Ridge National Laboratory Report ORNL/TM-2016/43. 2016.

[14] Cacuci DG. Sensitivity and Uncertainty Analysis: Theory. Volume 1. Chapman & Hall/CRC. 2003.

[15] Margulis M. Analysis of safety and performance parameters of the ESFR-SMART core at end of cycle. ESFR-SMART Project Deliverable D1.2.2. 2020.

[16] Bécares V. Report on Sensitivity Analysis Methods. SANDA Project Deliverable D5.1. 2021.

[17] Jiménez-Carrascosa A, García Herranz N, Cabellos O. On the characterization of biases arising from methods and approximations used for sensitivity analyses. International Conference on Physics of Reactors 2022 (PHYSOR 2022) Pittsburgh, PA (USA). 15-20 May. 2022.

[18] Jiménez-Carrascosa A, Cabellos O, Díez CJ, García-Herranz N. Processing of JEFF nuclear data libraries for the SCALE Code System and testing with criticality experiments. Spanish Nuclear Society Annual Meeting. Granada (Spain). 2021.

[19] Panizo S, Bécares V, Leclaire N, Jiménez-Carrascosa A, García-Herranz N, Romojaro P, et al. Comparison of Sensitivity/Uncertainty analysis methodologies in the European Sodium Fast Reactor. Spanish Nuclear Society Annual Meeting. Granada (Spain). 2021.

[20] Werner CJ. MCNP6 User's Manual, Code version 6.2. Los Alamos National Laboratory Report LA-UR-17-29981. 2017.

[21] Hurwitz H. Naval Reactors Physics Handbook - Volume I. Nav. React. Div. React. Dev. United States At. Energy Comm., vol. I. 1964.

[22] Kiedrowski BC, Brown FB, Wilson PPH. Adjoint-Weighted Tallies for k-Eigenvalue Calculations with Continuous-Energy Monte Carlo. Nuclear Science and Engineering. 2011;168:226-41.

[23] Truchet G, Leconte P, Santamarina A, Brun E, Damian F, Zoia A. Computing adjoint-weighted kinetics parameters in Tripoli-4® by the Iterated Fission Probability method. Annals of Nuclear Energy. 2015;85:17-26.

[24] Shi G, Jia C, Guo X, Li K, Wang K, Huang S, et al. Improved generalized perturbation theory method for sensitivity analysis of generalized response function. Progress in Nuclear Energy. 2021;134:103643.

[25] Perfetti CM. NE499/515 - Lecture 17: Sensitivity Analysis in Nuclear Criticality Safety. Nucl. Eng. Lect. 2022.

[26] Aufiero M, Bidaud A, Hursin M, Leppänen J, Palmiotti G, Pelloni S, et al. A collision history-based approach to sensitivity/perturbation calculations in the continuous energy Monte Carlo code SERPENT. Annals of Nuclear Energy. 2015;85:245-58.

[27] Dyrda J, Soppera N, Hill I, Bossant M, Gulliford J. New features and improved uncertainty analysis in the NEA nuclear data sensitivity tool (NDaST). EPJ Web Conf. 2017;146:06026.

[28] Romojaro P, Álvarez-Velarde F, García-Herranz N. SUMMON: Sensitivity and Uncertainty Methodology for MONte carlo Codes. M&C 2017 - International Conference on Mathematics & Computational Methods Applied to Nuclear Science & Engineering. Jeju (Korea). 16-20 April. 2017.
[29] NJOY21. NJOY21—NJOY for the 21st Century. https://www.njoy21.io. 2022.
[30] Romojaro P. Nuclear data analyses for improving the safety of advanced lead-cooled reactors. PhD Thesis: Universidad Politécnica de Madrid; 2019.
[31] Romojaro P, Álvarez-Velarde F, García-Herranz N. Sensitivity methods for effective delayed neutron fraction and neutron generation time with summon. Annals of Nuclear Energy. 2019;126:410-8.
[32] Mikityuk K, Krepel J, Girardi E. ESFR-SMART: New Horizon-2020 project on SFR safety. International Conference on Fast Reactors and Related Fuel Cycles: Next Generation Nuclear Systems for Sustainable Development (FR17) Programme and Papers. International Atomic Energy Agency (IAEA)2017. p. v.
[33] Fiorini GL, Vasile A. European Commission – 7th Framework Programme: The Collaborative Project on European Sodium Fast Reactor (CP ESFR). Nuclear Engineering and Design. 2011;241:3461-9.
[34] Fridman E, Álvarez Velarde F, Romojaro Otero P, Tsige-Tamirat H, Jiménez Carrascosa A, García Herranz N, et al. Neutronic Analysis of the European Sodium Fast Reactor: Part I—Fresh Core Results. Journal of Nuclear Engineering and Radiation Science. 2021;8.
[35] Buiron L, Sciora P, Rimpault G. Additional ASTRID benchmark. OECD/NEA WPRS SFR UAM. 2019.
[36] Fiorito L, Malambu E, Kennedy G, Fernandez R, Van den Eynde G. Novel neutronics design of the MYRRHA core. International Conference on Fast Reactors and Related Fuel Cycles FR22: Sustainable Clean Energy for the Future. Vienna (Austria). 19-22 April. 2022.
[37] Fiorito L, Hernandez-Solis A, Romojaro P, Stankovskiy A. Requested neutronics parameters for SU analysis of MYRRHA core. SCK CEN Report SCK CEN/45347165 2021.
[38] Grasso G, Petrovich C, Mattioli D, Artioli C, Sciora P, Gugiu D, et al. The core design of ALFRED, a demonstrator for the European lead-cooled reactors. Nuclear Engineering and Design. 2014;278:287-301.
[39] Castelluccio DM, Grasso G, Lodi F, Peluso VG, Mengoni A. Nuclear data target accuracy requirements for advanced reactors: The ALFRED case. Annals of Nuclear Energy. 2021;162:108533.
[40] Castelluccio DM, Lodi F, Peluso VG, Grasso G. Preliminary evaluation of ALFRED S/U analysis. OECD/NEA WPEC SG46. 2019.
[41] Grasso G, Lodi F, Romojaro P, Garcia-Herranz N, Alvarez-Velarde F, Lopez D, et al. Stress-testing the ALFRED design – Part I: Impact of nuclear data uncertainties on Design Extension Conditions transients. Progress in Nuclear Energy. 2018;106:372-86.
[42] Chiba G. Calculation of Effective Delayed Neutron Fraction Using a Modified k-Ratio Method. Journal of Nuclear Science and Technology. 2009;46:399-402.
[43] Bretscher MM. Perturbation-independent methods for calculating research reactor kinetic parameters. Argonne National Laboratory Report ANL/RERTR/TM-30. 1997.
[44] Cacuci DG. Handbook of Nuclear Engineering. Springer Science & Business. 2010.
[45] Fiorito L, Dyrda J, Fleming M. JEFF-3.3 covariance application to ICSBEP using SANDY and NDAST. EPJ Web Conf. 2019;211:07003.
[46] Hill I, Jeong S. Status and analysis of P1 angular scattering sensitivity data available with the database for ICSBEP (DICE). M&C 2017 - International Conference on Mathematics & Computational Methods Applied to Nuclear Science & Engineering. Jeju (Korea). 16-20 April.2017.
[47] Shibata K, Iwamoto O, Nakagawa T, Iwamoto N, Ichihara A, Kunieda S, et al. JENDL-4.0: A New Library for Nuclear Science and Engineering. Journal of Nuclear Science and Technology. 2011;48:1-30.

Annex

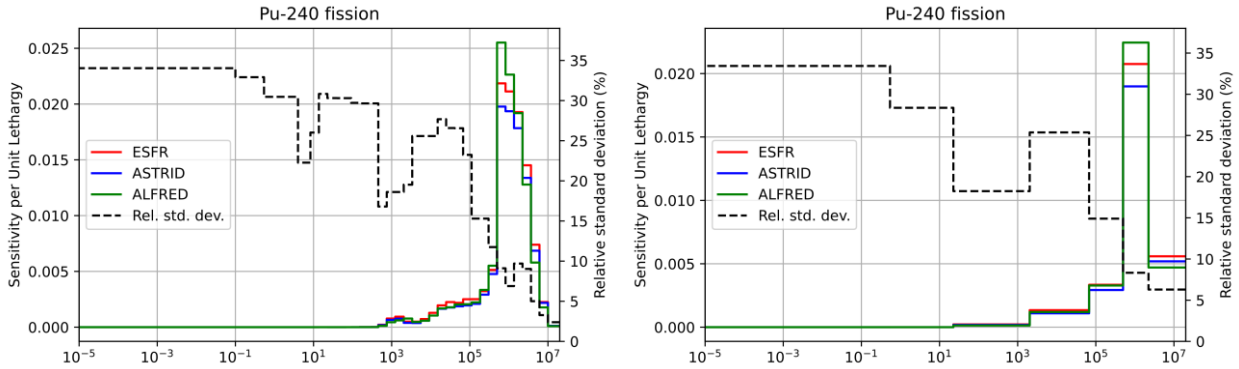

Figure A.1. 33- and 7-group multiplication factor sensitivity profiles of ^{240}Pu (n,f) for ESFR, ASTRID and ALFRED designs along with the uncertainty of the quantity in the JEFF-3.3 AMPX-formatted covariance matrix.

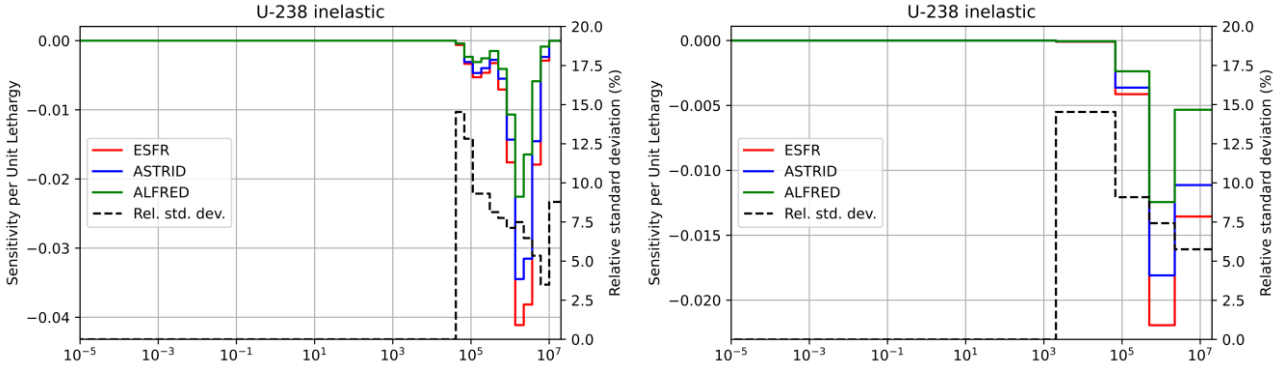

Figure A.2. 33- and 7-group multiplication factor sensitivity profiles of ^{238}U (n,n') for ESFR, ASTRID and ALFRED designs along with the uncertainty of the quantity in the JEFF-3.3 AMPX-formatted covariance matrix.

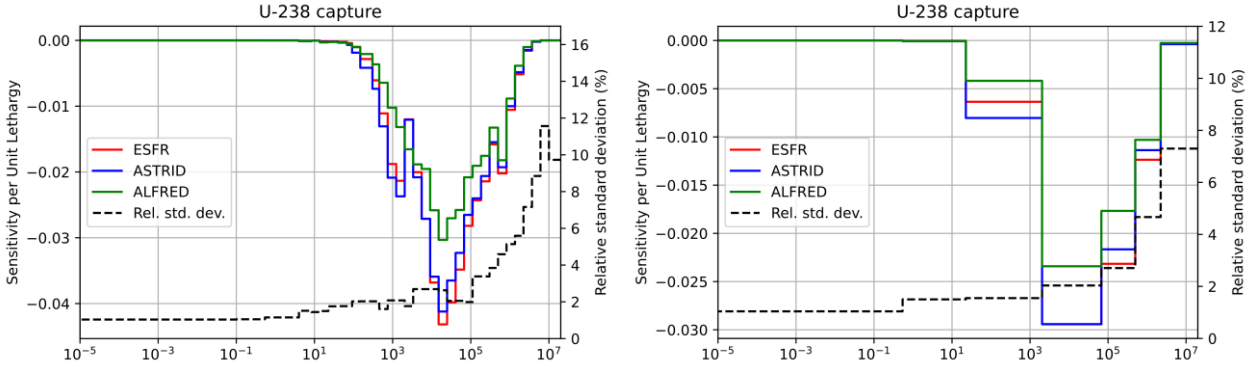

Figure A.3. 33- and 7-group multiplication factor sensitivity profiles of ^{238}U (n,γ) for ESFR, ASTRID and ALFRED designs along with the uncertainty of the quantity in the JEFF-3.3 AMPX-formatted covariance matrix.

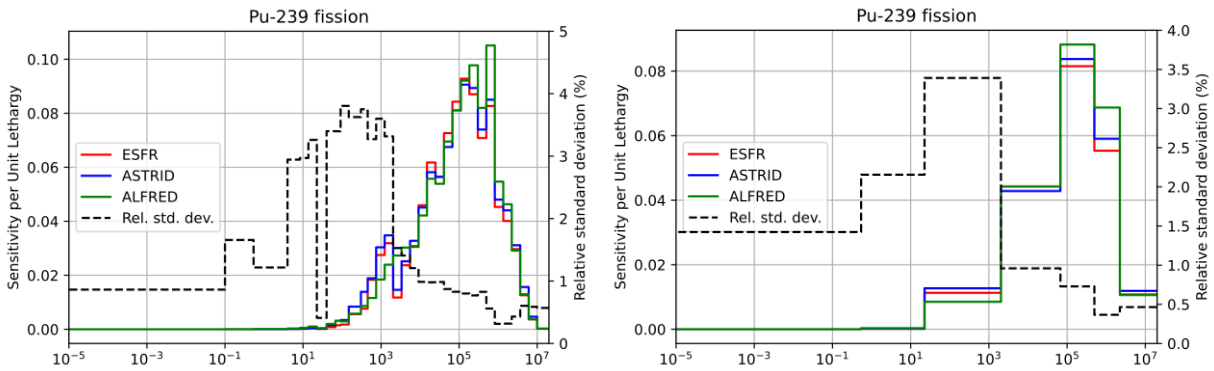

Figure A.4. 33- and 7-group multiplication factor sensitivity profiles of ^{239}Pu (n,f) for ESFR, ASTRID and ALFRED designs along with the uncertainty of the quantity in the JEFF-3.3 AMPX-formatted covariance matrix.

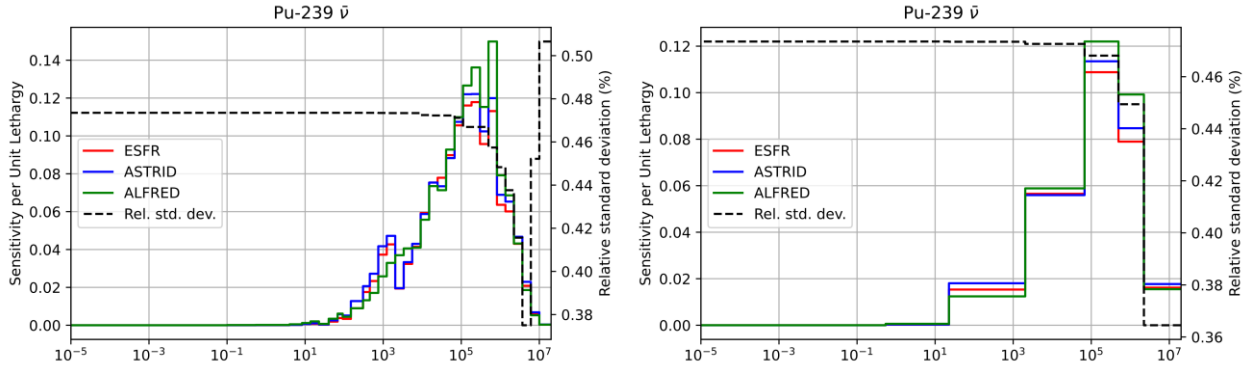

Figure A.5. 33- and 7-group multiplication factor sensitivity profiles of ^{239}Pu ν for ESFR, ASTRID and ALFRED designs along with the uncertainty of the quantity in the JEFF-3.3 AMPX-formatted covariance matrix.

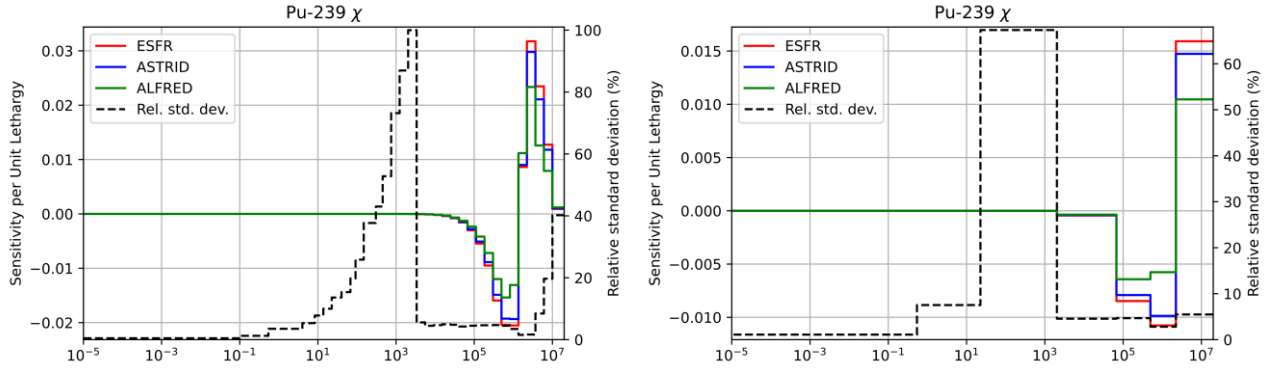

Figure A.6. 33- and 7-group multiplication factor sensitivity profiles of ^{239}Pu χ for ESFR, ASTRID and ALFRED designs along with the uncertainty of the quantity in the JEFF-3.3 AMPX-formatted covariance matrix.

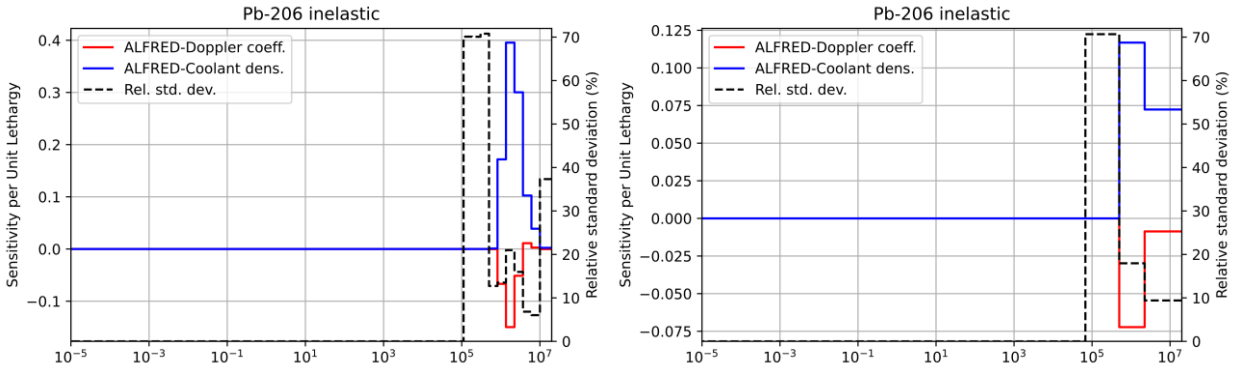

Figure A.7. 33- and 7-group Doppler and coolant density coefficients sensitivity profiles of ^{206}Pb (n,n') for ALFRED design along with the uncertainty of the quantity in the JEFF-3.3 AMPX-formatted covariance matrix.

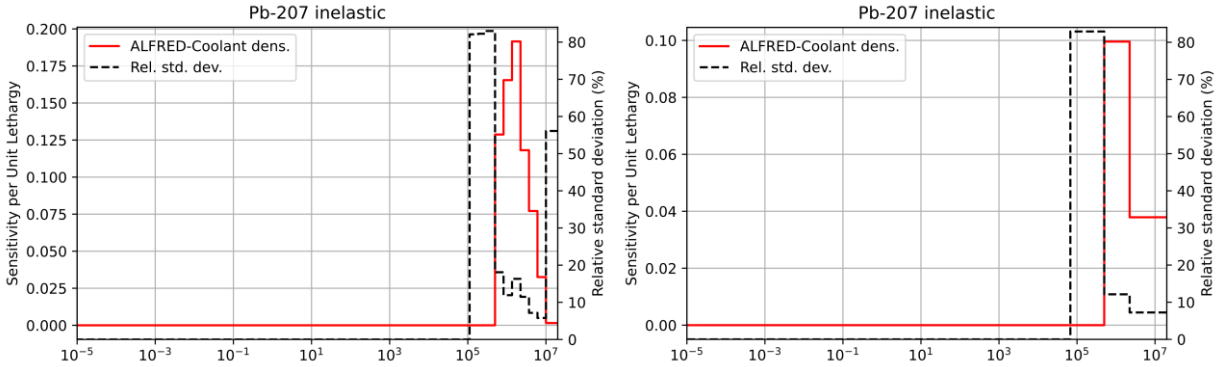

Figure A.8. 33- and 7-group coolant density coefficient sensitivity profiles of ^{207}Pb (n,n') for ALFRED design along with the uncertainty of the quantity in the JEFF-3.3 AMPX-formatted covariance matrix.

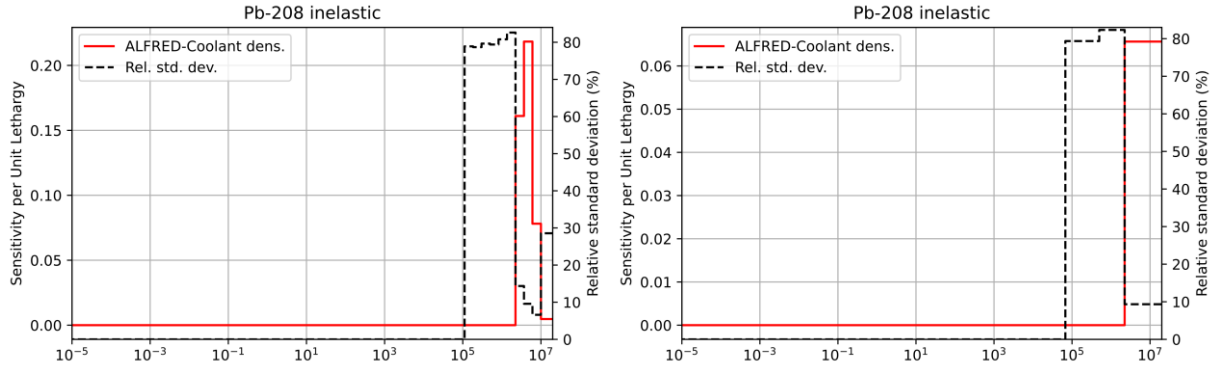

Figure A.9. 33- and 7-group coolant density coefficient sensitivity profiles of ^{208}Pb (n,n') for ALFRED design along with the uncertainty of the quantity in the JEFF-3.3 AMPX-formatted covariance matrix.

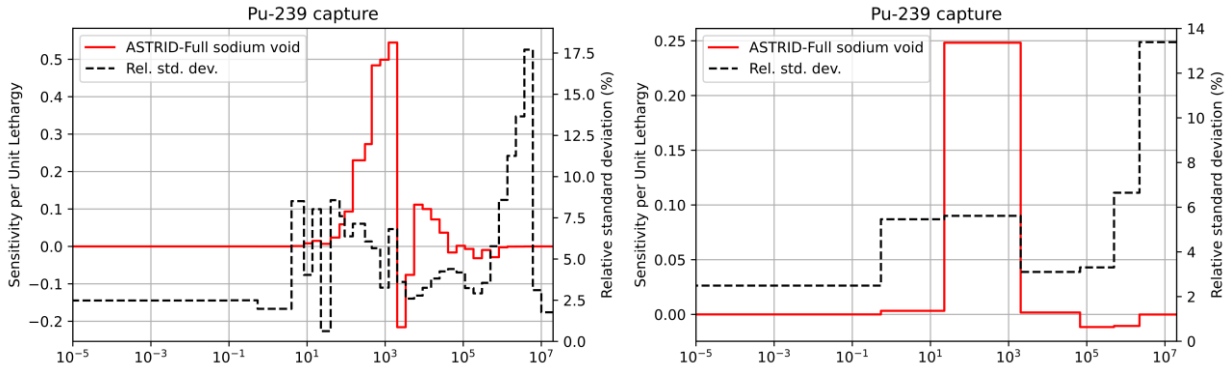

Figure A.10. 33- and 7-group full sodium void coefficient sensitivity profiles of ^{239}Pu (n,γ) for ASTRID design along with the uncertainty of the quantity in the JEFF-3.3 AMPX-formatted covariance matrix.

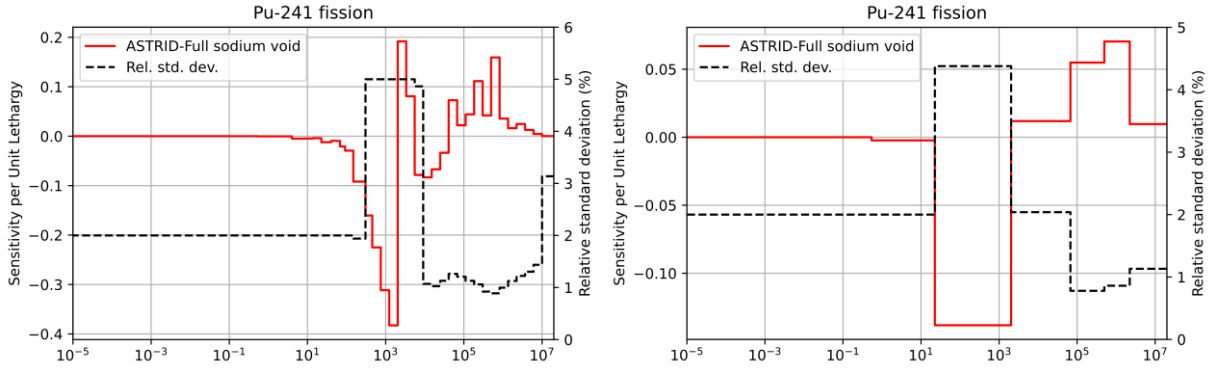

Figure A.11. 33- and 7-group full sodium void coefficient sensitivity profiles of ^{241}Pu (n,f) for ASTRID design along with the uncertainty of the quantity in the JEFF-3.3 AMPX-formatted covariance matrix.

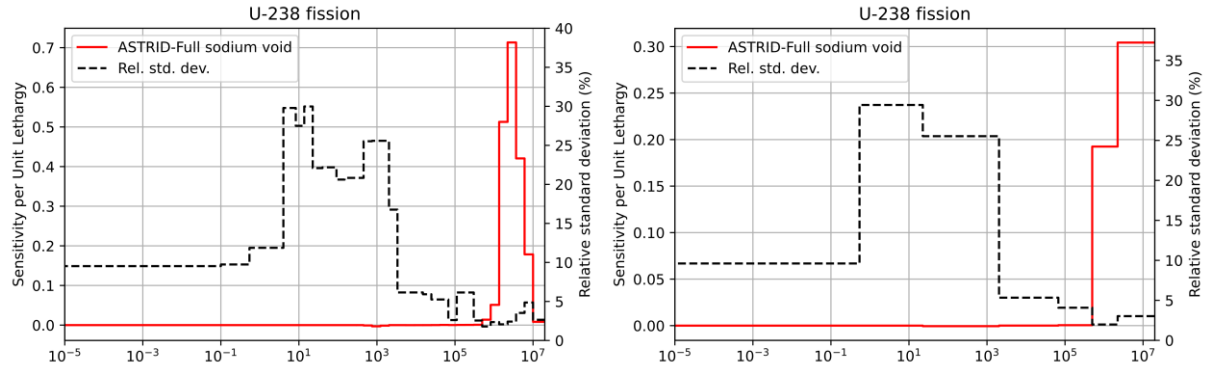

Figure A.12. 33- and 7-group full sodium void coefficient sensitivity profiles of ^{238}U (n,f) for ASTRID design along with the uncertainty of the quantity in the JEFF-3.3 AMPX-formatted covariance matrix.

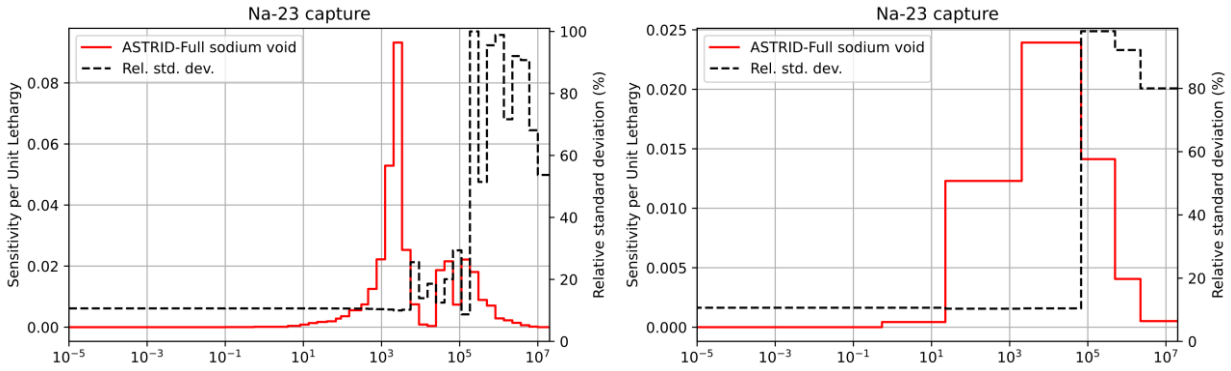

Figure A.13. 33- and 7-group full sodium void coefficient sensitivity profiles of ^{23}Na (n,γ) for ASTRID design along with the uncertainty of the quantity in the JEFF-3.3 AMPX-formatted covariance matrix.

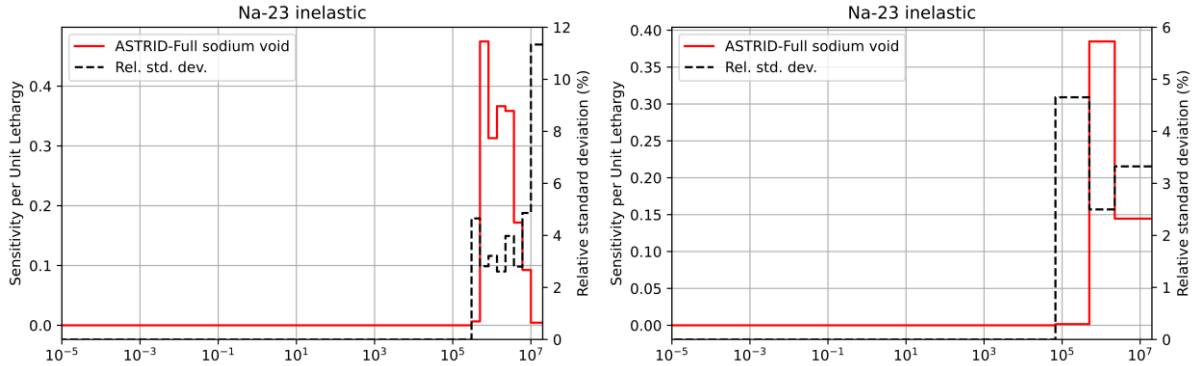

Figure A.14. 33- and 7-group full sodium void coefficient sensitivity profiles of ^{23}Na (n,n') for ASTRID design along with the uncertainty of the quantity in the JEFF-3.3 AMPX-formatted covariance matrix.

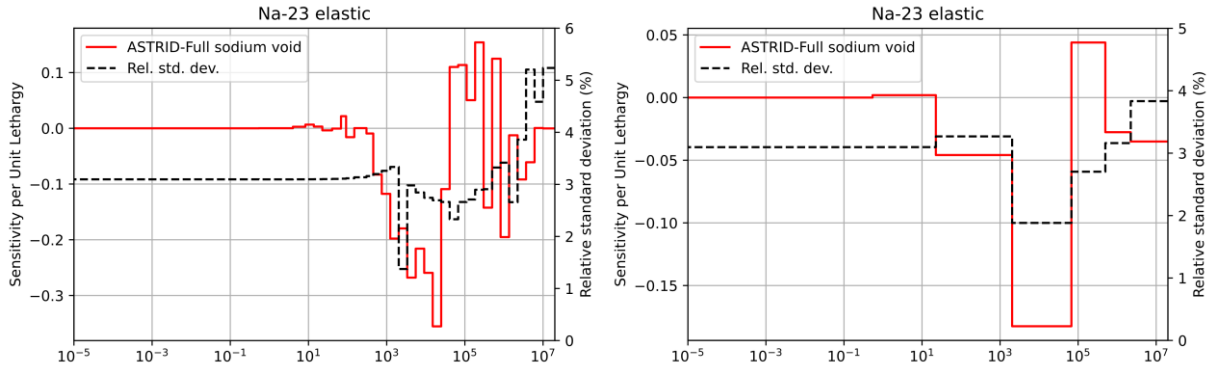

Figure A.15. 33- and 7-group full sodium void coefficient sensitivity profiles of ^{23}Na (n,n) for ASTRID design along with the uncertainty of the quantity in the JEFF-3.3 AMPX-formatted covariance matrix.

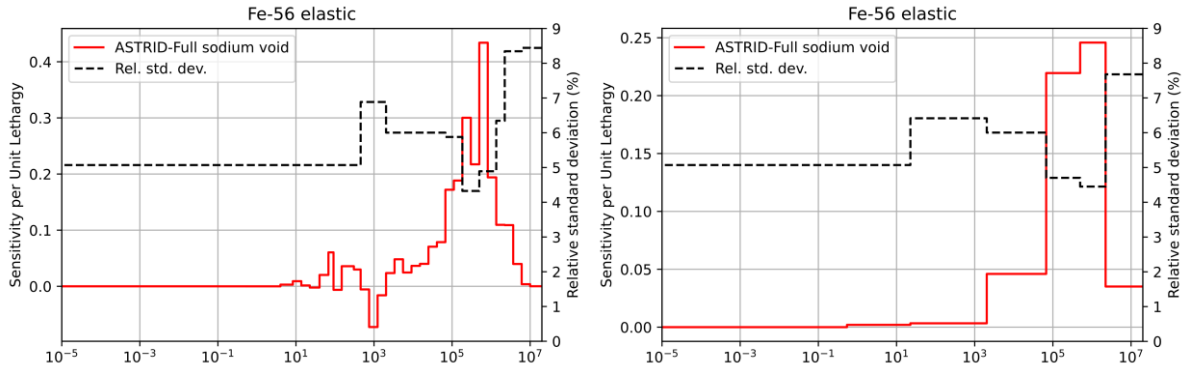

Figure A4.16. 33- and 7-group full sodium void coefficient sensitivity profiles of ^{56}Fe (n,n) for ASTRID design along with the uncertainty of the quantity in the JEFF-3.3 AMPX-formatted covariance matrix.

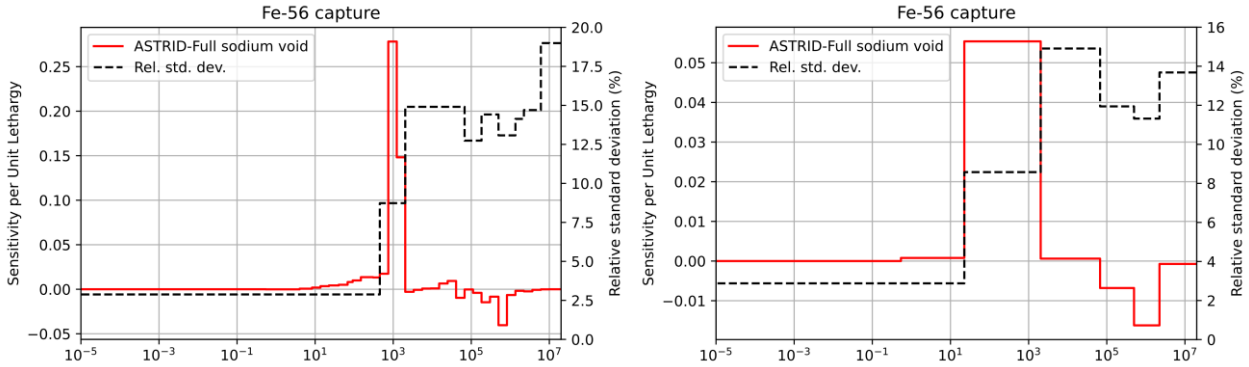

Figure A.17. 33- and 7-group full sodium void coefficient sensitivity profiles of ^{56}Fe (n,γ) for ASTRID design along with the uncertainty of the quantity in the JEFF-3.3 AMPX-formatted covariance matrix.